Preferential cavitation and friction-induced heating of multi-component Diesel fuel surrogates up to 450MPa

Alvaro Vidal[1,*], Konstantinos Kolovos[1,2], Martin R. Gold[3], Richard J. Pearson[3], Phoevos Koukouvinis[1], Manolis Gavaises[1]

[1]City University London – Northampton Square, London EC1V 0HB, United Kingdom

[2]Perkins Engines Company Ltd – Peterborough PE1 5FQ, United Kingdom

[3]BP Formulated Products Technology, Pangbourne, UK

*Corresponding author: alvaro.vidal-roncero@city.ac.uk

Abstract

The present work investigates the formation and development of cavitation of a multicomponent Diesel fuel surrogate discharging from a high-pressure fuel injector operating in the range of injection pressures from 60MPa to 450MPa. The compressible form of the Navier-Stokes equations is numerically solved with a density-based solver employing the homogeneous mixture model for accounting the presence of liquid and vapour phases, while turbulence is resolved using a Large Eddy Simulation approximation. Simulations are performed on a tapered heavy-duty Diesel engine injector at a nominal fully-open needle valve lift of 350μm. To account for the effect of extreme fuel pressurisation, two approaches have been followed: (i) a barotropic evolution of density as function of pressure, where thermal effects are not considered and (ii) the inclusion of wall friction-induced and pressurisation thermal effects by solving the energy conservation equation. The PC-SAFT equation of state is utilised to derive thermodynamic property tables for an eight-component surrogate based on a grade no.2 Diesel emissions-certification fuel as function of pressure, temperature, and fuel vapour volume fraction. Moreover, the preferential cavitation of the fuel components within the injector's hole is predicted by Vapour-Liquid Equilibrium calculations; lighter fuel components are found to cavitate to a greater extent than heavier ones. Results indicate a significant increase of temperature with increasing pressures due to friction-induced heating, leading to a significant increase in the mean vapour pressure of the fuel and an increase of the mass of fuel cavitating, but at the same time to an unprecedented decrease of cavitation volume inside the fuel injector with increasing injection pressure. This has been attributed to the shift of the pressure drop from the feed to the back pressure inside the injection hole orifice as fuel discharges; as injection pressure increases, so does the pressure inside the orifice, confining the location of cavitation formation to a smaller volume attached to the upper part of orifice, thus restricting cavitation growth.

Keywords: cavitation, multicomponent, PC-SAFT, Diesel, thermal effects, preferential vaporisation

1. Introduction

The United Nations Environment Programme (UNEP) reported in November 2018 mentions that "pathways reflecting current nationally determined contributions imply global warming of about 3°C by 2100, with warming continuing afterwards" in its assessment of the Paris Agreement[1]. As the transport sector accounts for ~23% of the total Greenhouse Global Emissions[2], attempts have been made to study and find a means to reduce them, including utilisation of Diesel surrogates[3], additives in Diesel and bio-Diesel blends[4], multiple injections per power cycle[5] and increase in injection pressure[6]. Modern Diesel engines operate with upstream pressures of around 200MPa at full load, although the current trend is to increase them up to 300MPa, in accordance with the latest emission regulations. Experimental studies have been done regarding sprays at extreme injection pressures, up to 500MPa[7], reporting an increase in the spray tip penetration, better mixing, and flame stability, potentially driving towards a better combustion and less emissions. However, due to the micrometre scales of injectors, high injection pressures will irremediably cause very high fuel velocities which, combined with the sharp geometric changes in the injector passages, lead to local depressurisation with significant pressure gradients. If the pressure decreases beyond the fuel's saturation point, the fuel cavitates, which in turn, results to injector underperformance[8] while it is related to mass flux choke due to blocking of the free flow[9] and possible cavitation erosion. Despite this, cavitation can be beneficial when managed effectively, as it promotes liquid jet atomisation[10-14] increases the spray cone angle[15] and thus, mixing and combustion[16] is enhanced.

As cavitation measurements with real-size injectors operating pressures beyond 200MPa[17, 18] is not possible up to now, simulation models can offer further insight into the nozzle flow. Both the Volume of Fluid method (VOF)[19, 20] and the Homogeneous Equilibrium Model (HEM)[21] have been used to simulate the presence of the second phase due to cavitation and validated against relevant experiments at lower pressures[22]. Such models can be used to study the formation and transport of the vapour phase, the turbulent fluctuations in velocity and pressure and the effect of non-condensable gases[23]. It has been also possible to look into the effect of liquid and vapour compressibility on supercavitation formation[24].

An additional complexity related to the increase of injection pressure in modern fuel injection systems is related to the strong velocity gradients that induce wall friction, generating an important source of heating[25, 26]. Nonetheless, thermal effects are typically neglected in relevant simulation studies and the flow within the fuel injector is considered isothermal, while the thermodynamic properties of the fuel are assumed constant. However, as the pressure increases within the injector, significant changes to fuel physical properties are realised, which are critical in the formation of cavitation[27] and affect combustion and emissions[28]. With regards to liquid density variation, a barotropic evolution of the liquid density as function of pressure is frequently utilised[29]. A barotropic equation has been derived in past studies following Kolev's Diesel properties collection[30] or single component surrogates using the NIST Refprop[31] database. Such simplifications may lead to deviations in the discharge coefficient and fuel heating predictions with respect to the real fuel, particularly in cases of high pressure injections[25]. For the vapour phase, the usual assumption adopted is the ideal gas law behaviour.

Real Diesel fuels are typically composed of hundreds of components, which cannot be addressed using constant properties or a simplified equation of state (EoS). Composition effects in Diesel fuel are related to changes in the spray atomisation[32] and spray tip penetration[33], but the cavitation of each component in the multicomponent fluid during injection has not been addressed. There is only one related study in which the effect of non-condensable gas on cavitation of a single component fuel during injection is analysed[34], modelled with a cubic EoS. Experiments of Diesel and biodiesel fuel mixtures have shown that the biodiesel content slows down cavitation due to its higher molar weight[35], which was also seen numerically at extreme temperatures[36]. Still, most studies regarding preferential cavitation and transport based on the solution of the full Navier-Stokes equations are based on models for fuel droplets in a gaseous environment[37-39].

In an effort to simulate in a more accurate way the effect of fuel property variation at different conditions for multi-component fuels, the PC-SAFT equation of state[40] can be used. This is a theoretically derived model, based on the perturbation theory[41-44], that requires only three molecular-based parameters per component for fluid property calculations. There are several advantages in using the PC-SAFT compared to a cubic equation of state for calculating fluid properties. The PC-SAFT predicts derivative properties (such as the speed of sound) with satisfactory accuracy, reducing errors by a factor of up to eight[45, 46], as compared to predictions with a cubic equation of state (such as the Peng-Robinson[47] or Soave-Redlich-Kwong[48]). Density predictions with the PC-SAFT exhibit six times lower error for a widely used surrogate such as dodecane[49] and half the error of those made with improved cubic equations, such as volume-translated versions[50]. The PC-SAFT provides satisfactory agreement between calculated and experimental properties of reservoir fluids[51] and natural gas[52].

The aim of the current work is to investigate the in-nozzle flow and cavitation forming in heavy-duty Diesel injector at injection pressures up to 450MPa, using a realistic multicomponent Diesel surrogate. This surrogate is a mixture of eight components based on the composition of a grade no. 2-D S15 Diesel emissions certification fuel from Chevron-Phillips Chemical Co.[53], already modelled by the authors using the PC-SAFT[54]. The surrogate mass composition is listed in Table 1. Two different methodologies have been utilised: one neglecting the thermal effects and one where the energy equation is solved considering thermal effects due to wall-induced friction and fuel depressurisation. To the best of the author's knowledge, this is the first study in the literature where the PC-SAFT is utilised in nozzle flow simulations addressing the preferential cavitation of the fuel components and their evolution at extreme injection pressures.

Compound Name	$M_w\ [g/mol]$	$T_b[K]$	$z_i[\%\ mass]$	$m_i[-]$	$\sigma[\text{Å}]$	$\epsilon/k_B[K]$
n-octadecane	254.5	590.0	27.3082	7.438	3.948	254.90
n-hexadecane	226.4	560.0	3.2477	6.669	3.944	253.59
heptamethylnonane	226.4	520.0	35.1237	5.603	4.164	266.46
1-methylnaphthalene	142.2	518.0	10.8772	3.422	3.901	337.14
n-butylcyclohexane	140.3	456.2	10.8149	3.682	4.036	282.41
trans-decalin	138.2	460.5	4.0392	3.291	4.067	307.98
tetralin	132.2	480.9	3.8009	3.088	3.996	337.46
1,2,4-trimethylbenzene	120.2	442.6	4.7883	3.610	3.749	284.25

Table 1. Mass composition for the Diesel surrogate modelled on this work. Boiling points at 0.1 MPa taken from the literature.

Following the above brief introduction, the next section gives the outline of the case set-up, the geometry and CFD model used for the simulations. The results are shown including the internal flow, the effects on temperature due to friction and the preferential vaporisation of the components within the multicomponent mixture. Lastly, the final section gives a summary and critique of the findings.

2. Numerical Method

2.1. CFD model

The in-house density-based CFD codes used in this work solves the compressible Navier-Stokes equations utilising the open-access OpenFOAM[55] platform. The two-phase flow is assumed to be a homogeneous mixture of vapour and liquid in mechanical equilibrium, i.e. both phases share the same pressure and velocity fields. This implies that as there is only one fluid in the entire domain, the discharge is on liquid; this configuration resembles that of injector test benches, where fuel is squirted for thousands of hours into a liquid-filled collector. The barotropic behaviour of the fluid does not consider the energy conservation equation. The second thermodynamic closure solves for both the Navier-Stokes system and the energy conservation equation. Both solvers share a system which consists of the continuity equation:

$$\frac{\partial \rho}{\partial t} + \nabla \cdot (\rho \boldsymbol{u}) = 0 \tag{1}$$

Where ρ is the mixture density and $\boldsymbol{u}$ the velocity vector field, and the momentum equations:

$$\frac{\partial (\rho \boldsymbol{u})}{\partial t} + \nabla \cdot (\rho \boldsymbol{u} \otimes \boldsymbol{u}) = -\nabla p + \nabla \cdot \boldsymbol{\tau} \tag{2}$$

where p is the pressure and $\boldsymbol{\tau}$ is the stress tensor defined as $\boldsymbol{\tau} = \mu_{eff}[\nabla \boldsymbol{u} + (\nabla \boldsymbol{u})^T]$, with μ_{eff} defined as the sum of laminar, μ given by the thermodynamic table, and turbulent, μ_T, dynamic viscosities. Regarding the turbulence model, a Large Eddy Simulation (LES) model is used[56, 57]. In particular, the turbulent viscosity is modelled using the Wall Adaptive Large Eddy (WALE) model[58], by the equation:

$$\mu_t = \rho {L_s}^2 \frac{\left({S_{ij}}^d {S_{ij}}^d\right)^{3/2}}{\left(S_{ij} S_{ij}\right)^{5/4} + \left({S_{ij}}^d {S_{ij}}^d\right)^{5/4}} \tag{3}$$

where S_{ij} is the rate of strain tensor and ${S_{ij}}^d$ is the traceless symmetric part of the square of the strain of the velocity gradient tensor, i.e.:

$${S_{ij}}^d = \frac{1}{2}\left({g_{ij}}^2 + {g_{ji}}^2\right) - \frac{1}{3}\delta_{ij} {g_{kk}}^2 \tag{4}$$

With, $= \frac{\partial u_i}{\partial x_j}$ and δ_{ij} the Kronecker delta. The length scale, L_s, is based on the filter size and the cell to wall distance, d_{wall}, as follows:

$$\mathrm{L} = min\left\{\kappa\, d_{wall}, C_w\, V^{1/3}\right\} \tag{5}$$

where the used model constants are: κ the von Karman constant, 0.41, and C_w = 0.325. The energy conservation equation is also solved:

$$\frac{\partial (\rho E)}{\partial t} + \nabla \cdot (\rho \boldsymbol{u} E) = -\nabla \cdot (p \boldsymbol{u}) + \nabla \cdot (\tau \cdot \boldsymbol{u}) - \nabla \cdot (k_T \nabla T) \tag{6}$$

where E is the specific total energy of the system, defined as internal energy plus the kinetic energy, i.e. $E = h - \frac{p}{\rho} + \frac{|\boldsymbol{u}|^2}{2}$ where h is the enthalpy, and k_T the thermal conductivity of the fluid given by the thermodynamic tables.

Hybrid flux model

Two-phase flows are characterised, among others, by large variations in the speed of sound. While the speed of sound in the liquid phase is of the order of $O(10^3)\mathrm{m/s}$ and that of gas is $O(10^2)\mathrm{m/s}$, in the liquid-vapour mixture it drops down to

$O(1)$m/s. Therefore, for a typical velocity at the orifice of $O(10^2)$m/s, it can be expected a range in the Mach number from $O(10^{-1})$ to $O(10^2)$ m/s. For density-based solvers, low Mach numbers are causing convergence problems and dispersion, so a hybrid flux is used for accounting for both low and high Mach numbers. That, in terms of the interface pressure within the approximated Riemann solver scheme is:

$$p = [1 - \beta(M)]p^{inc} + \beta(M)p^{comp} \tag{7}$$

where

$$p^{inc} = \frac{C^L p^R + C^R p^L}{C^L + C^R} \tag{8}$$

$$p^{comp} = \frac{C^L p^R + C^R p^L + C^R C^L (u^L - u^R)}{C^L + C^R} \tag{9}$$

where $C = \rho c$ is the acoustic impedance, u is the interface velocity, L and R refer to the left and right side of the interface and:

$$\beta(M) = 1 - e^{-aM} \tag{10}$$

where a is a blending coefficient, set to 1.5. Thus $\beta(M) \to 0$ when $M \to 0$, and therefore $p = p^{inc}$. On the other hand, $\beta(M) \to 1$ when $M \to \infty$, and therefore $p = p^{comp}$.

2.2. Injector geometry and operating conditions

The examined injector geometry was based on a common rail 5-hole tip injector with tapered holes. The most important dimensions for this injector are shown in Table 2. The nominal mass flow rate at a reference condition of P_{inj}=180MPa has been also included. Although the simulation is transient, the needle valve was assumed to be still at its full lift of 350μm during the main injection stage. The simulated geometry considers only one fifth of the full injector geometry, as shown in Figure 1, imposing periodic boundary conditions on the symmetry planes. A hemispherical volume is attached to the nozzle exit; this volume is added in order to be able to capture the cavitation cloud inside the nozzle and avoid interference with the outlet boundary. Characteristic volumes of the injector geometry are also pointed out by colour in Figure 1(a); the walls are assumed to be adiabatic. Constant pressure boundary conditions of 60, 120, 180, 250, 350 and 450MPa at the inlet and 5MPa at the outlet have been considered. The temperature at the inlet boundary is fixed and corresponds to that of an isentropic expansion from the reference point set at 5MPa and 324K, shown in Table 3. This reference temperature is chosen based on the theoretical outlet temperature for operation at a reference injection pressure of 180MPa and a discharge coefficient of unity, i.e. the ideal case without pressure losses, as calculated in[59] using the same geometry. The temperature at the outlet of the domain is calculated by the solver. Also, in Table 3 the calculated mean exit velocity, speed of sound on the liquid, Mach number and discharge coefficient for each injection pressure are indicated.

Geometrical characteristics		
Needle radius at inlet (mm)		1.711
Inlet orifice rounding (mm)		0.05
Orifice length (mm)		1.262
Orifice diameter (mm)	Entrance D_{in}	0.37
	Exit D_{out}	0.359
Sac volume (mm^3)		1.19
k-factor = (D_{in} - D_{out}), D in µm		1.1
Nominal mass flow rate at P_{inj} =180MPa (g/s)		41.32

Table 2. Dimension of the injector used for the simulations on this work and nominal flow rate at the reference condition of P_inj =180MPa.

157

$P_{inj}[MPa]$	T_{inlet} [K]	U_{exit} [m/s]	$c_{liquid}[m/s]$	$M_{liquid}[-]$	C_d
60	332	332.39	1128	0.2946	0.842
120	340	461.02	1066	0.4324	0.819
180	345	564.69	1057	0.5342	0.813
250	350	664.77	1045	0.6361	0.812
350	359	781.67	1012	0.7724	0.807
450	365	881.74	1001	0.8808	0.804

Table 3. For each injection pressure, inlet temperatures, mean exit velocity, speed of sound on the liquid, Mach number and discharge coefficient. Results come from simulations with thermal effects being considered.

158

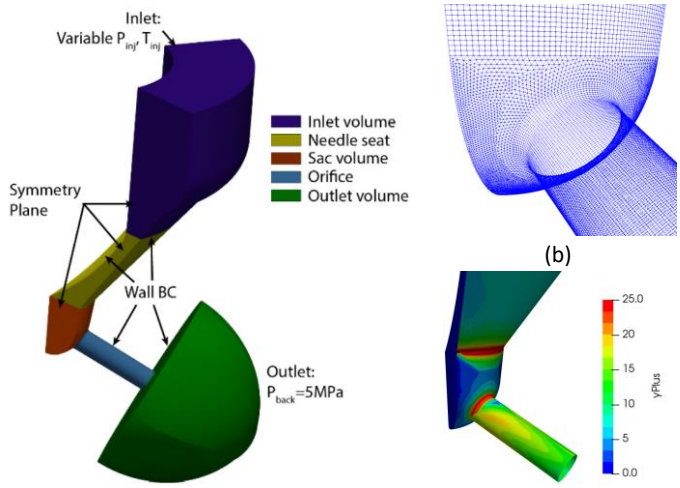

Figure 1. Simulated geometry (one fifth of the complete injector nozzle). Characteristic volumes are colourised, and the boundary conditions are indicated. The transition between the two distinct topologies at the orifice and the contour plot at P_{inj}=450MPa for the estimated y+ values are also added.

159

160 Regarding the computational mesh, two topologies have been used. As shown in Figure 1(b), upstream of the orifice entrance,
161 i.e. inside the nozzle's sac volume, an unstructured tetrahedral mesh is utilised. For the rest of the computational domain, a
162 hexahedral block-structured mesh is used. Given the flow conditions inside the injector nozzles, the Reynolds number at the
163 orifice, where cavitation develops, varies significantly between the cases. For 60MPa, it is ~35000, for 180MPa is ~60000 and
164 ~90000 for 450MPa. This corresponds to Taylor length scales, λ_g:

165 $$\lambda_g = \sqrt{10} Re^{-0.5} D \in (4\mu m, 6.5\mu m) \quad (11)$$

166 Where D is an indicative length of the geometry; in this case the nozzle hole exit diameter. The resolution in the core of the
167 orifice is ~5μm, with refinement near the walls down to a minimum cell size of ~2 μm. As also shown in Figure 1(c), for the

most restrictive case of 450MPa, the maximum y+ was 25. Due to the unfeasible computational effort a domain with a smaller cell size would entail, the near wall flow was treated with two wall functions: (i) kqRWallFunction[60] for the turbulent kinetic energy and (ii) nutkwallfunction[60] for the turbulent viscosity. The timestep was adapted to a fixed acoustic Courant number of 0.5, thus the timestep varied from 8ps for the 450MPa case to 100ps for the 60MPa case. Table 4 shows integral quantities of engineering interest, such as the overall mass and energy balance for each injection pressure, with thermal effects being considered. The last column in Table 4 shows the difference found in the mass flow rate at the exit for the most refined mesh, decreasing the smallest cell size to 1.06μm and, therefore, increasing the number of cells to 11M. No significant differences were found and therefore the 1.5M cells mesh was used for all following simulations.

	Mass flow rate $[g/s]$		**Energy flow rate** $[kJ/s]$		**%change in** $\dot{m}_{out}$ **after refinement**
$P_{inj}[MPa]$	$Inlet$	$Outlet$	$Inlet$	$Outlet$	
60	24.37	24.53	31.97	32.19	-
120	33.89	34.16	42.08	42.43	-
180	41.32	41.72	48.19	48.67	0.0528
250	49.06	49.38	53.91	54.28	0.0785
350	58.09	58.38	57.74	58.11	0.1169
450	66.31	66.59	59.17	59.44	0.1542

Table 4. Time-averaged mass and energy flow rates at the inlet and outlet for all cases, with thermal effects being considered. The last column shows the percentage change in mass flow rate at the outlet after a refinement from 1.5M to 11M cells for cases 180MPa to 450MPa, decreasing thus minimum cell size from 2.12μm to 1.06μm.

2.3. Thermodynamic properties

As already mentioned, the thermodynamic properties of the Diesel surrogate are modelled using the PC-SAFT EoS[61] for a density range of 0.001-1100kg/m3 and an internal energy range of -1.40779-4.7529MJ/kg in a tabulated format. The pure-component and ideal gas parameters can be found in the Tables A.1 and A.2 of the Appendix. The range in internal energy corresponds to temperatures in range of 280-2000K. These limits allow the correct characterisation of the vaporised and compressed fuel alike while also capturing the increased temperatures due to friction-induced heating. The structure of the table consists of 1000x1000 elements separated by constant intervals of the decimal logarithm (log10) of the density and internal energy. The properties are calculated every 0.006047 log10(kg/m^3) and 6.16696kJ/kg. For the barotropic approach, the properties were calculated maintaining the entropy of the fluid constant to that obtained at 324K and the imposed outlet pressure of 5MPa. Figure 2 shows the properties that govern the behaviour of the Diesel surrogate with respect to pressure following different isentropic curves, depending on the assumed reference temperature. While the black line refers to the one used in the barotropic approach, the other two refer to reference temperatures of: (i) 384K that is the maximum temperature reached in the liquid-vapor equilibrium phase for P_{inj}=180MPa considering thermal effects, and (ii) 484K that is the maximum temperature reached in the liquid-vapor equilibrium regime for P_{inj}=450MPa when thermal effects were considered.

As shown in Figure 2, at higher temperatures the values for density, viscosity and thermal conductivity decrease, while increasing the heat conductivity. Regarding density, an exponential-like increase can be seen in the liquid phase converging

at very high pressures for the distinct reference temperatures. It can also be seen a sudden increase in density at the saturation pressure, as the phase change is almost isobaric. Moreover, this saturation pressure changes significantly for the different cases, increasing with the reference temperature. This increase can be explained by the temperatures observed in Figure 2(b). For a higher temperature, the easier it is for the substance to evaporate and therefore its vapour pressure is enhanced. The change in temperature from vapour to liquid is seen smoother than for density. The vapour volume fraction shown in Figure 2 (c) highlights that the phase change is almost isobaric at bubble point, i.e. at low vapour volume fraction, while needing an additional pressure drop to complete the vaporisation. The dynamic viscosity, shown in Figure 2(d), shows how dependent it is on pressure, while it is inversely proportional with temperature. Figure 2(e) shows how significantly smaller the thermal conductivity is in the vapour phase compared to that of the liquid phase (of the order of O(100)), which will contribute to the vapour heating up more rapidly than the liquid. Similarly, another factor that will contribute to a faster heating up of the vapour is the heat capacity, shown in Figure 2(f), due to its lower values compared to those of the liquid phase.

The calculation of the vapour volume fraction α_v is determined by minimizing the Helmholtz Free Energy, according to the algorithm recently presented by the authors in[62], consisting on a stability analysis followed by a phase equilibrium calculation in case the mixture is found unstable. For the conditions studied in these isentropic simulations, the vapour pressure for the isentropic Diesel fuel is predicted to be 230Pa. For the case where the complete thermodynamic range is resolved, the saturation pressure is not fixed and will depend as well on the internal energy. The speed of sound c is calculated for a single phase directly from its definition:

$$c = \sqrt{\left(\frac{\partial p}{\partial \rho}\right)_s} \tag{12}$$

Where the subscript s indicates that the derivative is computed at constant entropy. When the fluid is in the two-phase region, the speed of sound follows the Wallis' rule[63]:

$$\frac{1}{\rho c^2} = \frac{\alpha_v}{\rho_v c_v^2} + \frac{1-\alpha_v}{\rho_l c_l^2} \tag{13}$$

where the subscripts v and l stand for vapour and liquid phase.

The dynamic viscosity, μ, is calculated by using an entropy scaling method[64], while the mixing rule is taken from the author's previous work[62]. The parameters used for the calculation of viscosity are found in Table A.3 of the Appendix. In the case of the two-phase region, the homogeneous viscosity is calculated with the expression[65]:

$$\mu = (1-\alpha_v)\left(1+\frac{5}{2}\right)\mu_l + \alpha_v \mu_v \tag{14}$$

Regarding the thermal conductivity, it is also calculated using the entropy scaling method[66]. The parameters used for its calculation can be also found in the Appendix, on Table A.4. A simple weighted mixing rule with the vapour volume fraction is used:

$$k_T = (1-\alpha_v)\, k_{T,l} + \alpha_v\, k_{T,v} \tag{15}$$

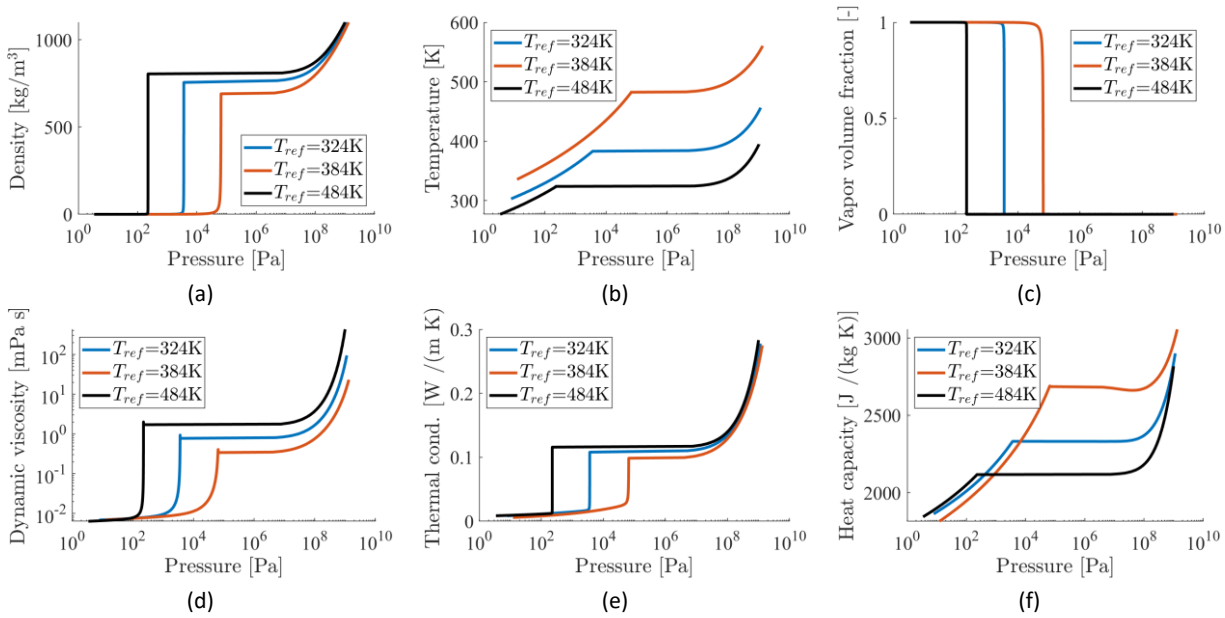

Figure 2. Thermodynamic data following an isentropic expansion of the Diesel surrogate. Three cases are shown depending on the reference temperature at 5MPa: (i) 324K for the barotropic method used in this work, (ii) 384K as the maximum temperature reached in the liquid-vapor equilibrium phase for P_{inj}=180MPa considering thermal effects, and (iii) 484K as the maximum temperature reached in the liquid-vapor equilibrium phase for P_{inj}=450MPa considering thermal effects.

2.4. Limitations, link to previous works and present contribution

Limitations arising from both the validity of the models themselves utilised and the selection of the specific conditions investigated, include: (1) the lack of detailed validation against experimental data for the extreme pressure values tests; (2) the dependency/accuracy of the simulations on the equations describing the fuel properties as function of pressure and temperature; (3) the assumption of local mechanical and thermal equilibrium, i.e. vapour and liquid have, locally, the same velocity (no slip) and same temperature, utilised in order to predict the amount of fuel that cavitates; and (4) the omission of transient effects ought to the movement of the injector's needle valve as well as the dependency of the obtained results on the specific geometry investigated here. A short evaluation of those factors is provided below before the presentation of the results obtained.

(1) With regards to the lack of experimental validation for the conditions tested, several comments and reference to prior studies can be made. For injection pressures up to 500MPa only spray formation results have been reported[7], but without information about the in-nozzle flow. As stated in the introduction, cavitation measurements in real-size injectors operating pressures beyond 200MPa[17] has not been possible up to now, due to transparent material constrains. Even for lower pressure conditions, only qualitative images have been obtained but not quantitative data for the cavitation volume fraction or the velocity field. Nevertheless, validation works have been thoroughly reported at lower injection pressures utilising similar models to those reported here. More specifically, homogeneous mixture models (either barotropic or mass transfer) have been found to have very similar performance[57, 67] in the limit of large mass transfer rates of the former. Also, such models have been validated for predicting the 3D distribution of vapor fraction within the validation uncertainty (±7%, including both numerical and experimental uncertainties). Further validation has been obtained for the flow field distribution, cavitation

shedding frequency and turbulent velocities in the same single-hole injector against high energy X-ray phase contrast imaging (XPCI) measurements for conditions covering a range of cavitation regimes (incipient, fully developed and vortex/string cavitation)[68, 69]. Additionally, validation against Laser Doppler Velocimetry (LDV) measurements have been also reported in[57, 70] utilising the WALE LES model for turbulence, suggest that it can reproduce the turbulent structures found in Diesel nozzles. These studies suggest that the model can capture both incipient and developed cavitation features. In the present study, the Reynolds number is ~[35000-90000] and thus, it is within the range of applicability of the selected model. As the vaporous core of cavitating vortices has been found to be in the order of 20μm[71], the smallest cell size of ~2μm used suggests that there are no under-resolved vortical structures that may cavitate and significantly influence the obtained results. For injection pressures in the range of 180MPa, the same simulated injector geometry was previously validated for predicting cavitation erosion damage[59] utilising the barotropic model. Cavitation erosion predictions have been also validated recently against measurements in a fuel pump[72]. These studies give confidence that the barotropic model is performing relatively well for similar cases as those studied here. Turning to thermal effects, there are no experiments available that can be used for validation. The earlier studies[73-76] from the authors performed also under both fixed needle valve conditions and including the movement of the injector's needle valve[77] have been compared results against 0-D predictions of the mean fuel heating up as it discharges through the fuel injector up to 300MPa, with very good accuracy[25, 26].

(2) A critical question relative to this study is related to the dependency/accuracy of the simulations on the equations describing the fuel properties as function of pressure and temperature. As mentioned, the simulations carried out have utilised properties derived by the PC-SAFT EoS. This EoS has been previously used with the Diesel surrogate of this work and compared with experimental results up to 500MPa and 600K for density, viscosity and volatility[78] with an accuracy of 1.7% for density, 2.9% in volatility and 8.3% in viscosity. Diesel fuels with different compositions have been also modelled at pressures up to 300MPa and temperatures up to 532K[79] and the obtained accuracy against those measurements was ~2% for density and ~10% for viscosity. Other Diesel properties, such as thermal conductivity, at extreme conditions up to 450MPa and 360K can also be found accurately predicted by PC-SAFT[80, 81] with an accuracy of 3%. It can thus be claimed that the selected EoS is a good compromise for studying such effects in high pressure injectors.

(3) One of the main assumptions in the described methodology is the mechanical and thermodynamic equilibrium between the liquid and the vapour phases. With regards to the mechanical equilibrium assumption, the recent study from the authors using a two-fluid model has confirmed that differences between liquid and vapour velocities are less than 10% and only in localised locations of the flow[82, 83]; they have been found not to affect the overall growth rate and production of vapour. The assumption of thermodynamic equilibrium is more significant. A metastable, i.e. non-thermodynamic equilibrium, state occurs when the pressure of the liquid drops below the saturation pressure and no vapour is formed due to the rapid expansion of the liquid[84, 85]. In the literature, non-thermodynamic equilibrium models, such as the well-known mass transfer models of Schnerr and Sauer[86], Singhal et al.[87] and Zwart et al.[88] are used. Predictions utilising such mass transfer models

tend towards equilibrium by increasing the evaporation/condensation coefficients[67, 89]. Apart from mass transfer models, in the literature there are models relying on the solution of the full Rayleigh-Plesset equation, commonly done in a Lagrangian reference frame, thus incorporating second order effects and the influence of surface tension. However, such models inherently assume a spherical bubble shape, the interaction between bubbles (break-up, coalescence) is not easy to describe and the coupling with the continuous phase (liquid) is difficult in areas of large void fractions[90-94]. The relaxation time of the tensile stresses, i.e. those acting in the metastable state, was numerically estimated to be of the order of 10ns in a flow configuration where a vertical tube filled with liquid was impacted vertically, leading to an expansion wave of 30MPa[95]. However, the nuclei concentration used in this study was infinitesimally small, which is not applicable to real systems and thus its result is a significant overprediction. Nevertheless, it is possible to use this time-scale to estimate that, as the residence time of the fluid in the injection hole has a minimum value of the order of 1μs, that for the 450MPa case, the time to reach equilibrium would be, at least, 100 times faster.

(4) Finally, the present work omits transient effects related to the motion of the needle valve[96], while it refers to only one injector geometry utilised with heavy-duty diesel engines featuring hole tapering. It has been reported in the literature that cavitation reduces the mixing uniformity within circular, sharp-edged orifices[97] while tapered nozzles reduce its appearance[98]. Thus, although the studied geometry is representative for such application, it can be expected that different cavitation volume fraction will be developing for other nozzle geometries. With regards to the needle valve motion, it is well documented in the literature that depending on the nozzle geometry and needle valve position, cavitation may appear to the bottom part of the injection hole as well as the needle seat area and inside the nozzle's sac volume at low needle lifts[99-101]. More recent studies have shown that the initial air/liquid distribution inside the nozzle volume prior to the start of injection are also complex, with large air bubbles been present[99, 101-103]; these are formed during the needle valve closure that induces back flow to the injector. However, such effects and flow regimes are not realised when the needle valve is at its nominal full lift position. At the same time, the needle remains still for a relatively large duration, typically more than 10times longer compared to the opening/closing time. Transient effects although important for cavitation erosion[104], nozzle wall wetting and formation of non-well atomised liquid fragments that can affect emissions are out of scope of the present work.

Despite those limitations, the present work aims to make the following contributions: To the best of the author's knowledge, this is the first study in the literature where the PC-SAFT is utilised in nozzle flow simulations addressing the preferential cavitation of the fuel components and their evolution at injection pressures up to 450MPa. For this, an 8-component Diesel surrogate[105] is modelled using the PC-SAFT EoS, considering the effects of variable thermal conductivity, heat capacity and viscosity due to extreme pressurisation. The authors also take advantage of PC-SAFT to calculate the individual vaporisation of each component within the vapour cloud during cavitation, as each component vaporises at a distinct rhythm, different to that of the mixture and to that of the other components.

3. Results

In this section, the results obtained for the range of injection pressures from 60MPa and up to 450MPa are presented. If not stated otherwise, all results consider thermal effects. Firstly, the internal flow through the injector is inspected. Secondly, the changes in temperature and vapour pressure are investigated and compared with the case where thermal effects are neglected. Thirdly, the formation of cavitation inside the nozzle orifice is analysed. Lastly, due to the multicomponent nature of the fuel, the preferential cavitation of its components is examined.

3.1. Flow field

Figures 3 through 5 show predictions of three time-averaged (i) magnitude of the vorticity on a logarithmic scale, (ii) density and (ii) viscosity at three injection pressures; results are presented in two sets of slices: one longitudinal to the injector geometry and four transversals to the nozzle hole. Thin solid black lines are added for clarity; all plots on each Figure share the same colour scale. Vorticity indicates locations where thermal effects become significant due to shearing. Lower values, of the order of 10^5/s or smaller, are seen in the core of the flow as it travels through the sac volume as well as into the orifice. Close to the walls, vorticity is generated reaching values up to 10^8/s, due to the large shear induced from the no-slip wall velocity boundary condition. High values of ~10^7/s are also found on a relatively wide region located on the top half of the orifice volume, where separation of the flow occurs, and cavitation is forming. Density and viscosity show similar behaviour throughout the injector. Inside the nozzle's sac volume, densities take values from 845 kg/m^3 for injection pressure of 60MPa, 900.342 kg/m^3 for 180MPa and up to 982.345 kg/m^3 for 450MPa. This density decreases as the fuel expands through the orifice down to ~720kg/m^3 at the exit of the orifice where the pressure is set to 50MPa. As the flow separates at the entrance of the injector orifice and the fuel cavitates, densities decrease locally 3 orders of magnitude, to ~10^{-3} kg/m^3, inducing strong density gradients. It can be also clearly seen that as injection pressure increases, the extend of low-density values for the valour-liquid mixture is significantly reduced, due to the gradual condensation of vapour caused by the increased pressures present inside the injection hole. The iso-surface of 50% vapour volume fraction is also depicted, showing for the 180 and 450MPa cases two coherent structures separated at the symmetry midplane; thorough discussion of the cavitation formation and development will be given in the following subsections. Regarding viscosity, the increase with injection pressure in the nozzle's sac volume is significantly higher than that for density. At 60MPa, the viscosity of the fuel is 2.66mPa·s, doubling to 5.2mPa·s at 180MPa and then quadrupling up to 19.64mPa·s at 450MPa. Average values at the nozzle exit are ~1.3mPa·s. Minimum values of $7 \cdot 10^{-3}$mPa·s are found again at the entrance of the orifice where the flow separates.

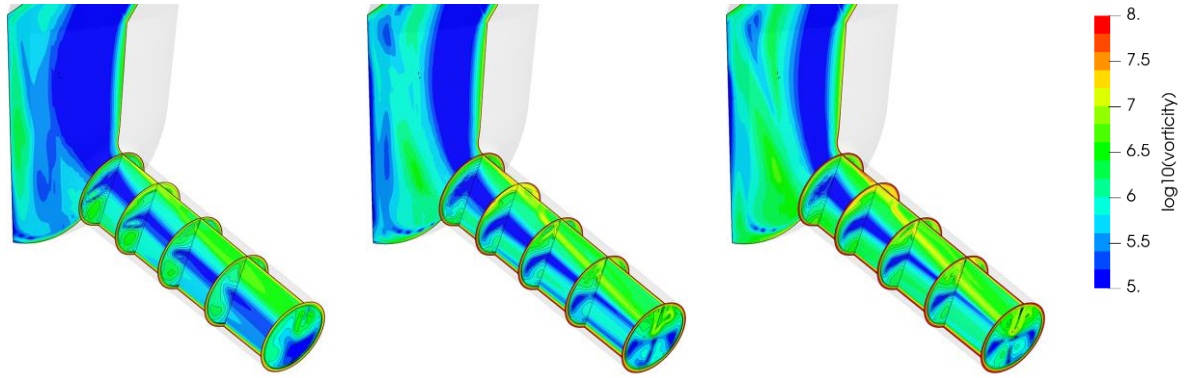

(a) 60MPa (b) 180MPa (c) 450MPa

Figure 3. Predicted time-averaged vorticity, in logarithmic scale, on different slices at the sac volume and orifice for three injection pressures. Thermal effects are considered.

345

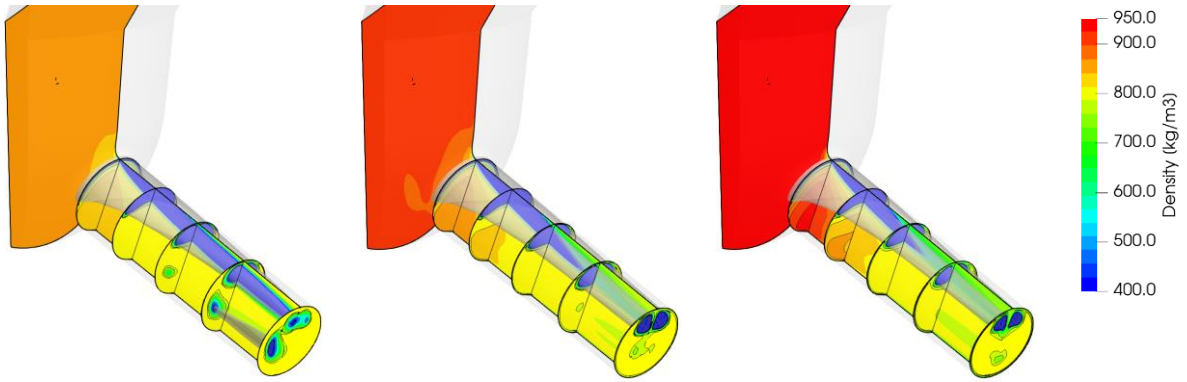

(a) 60MPa (b) 180MPa (c) 450MPa

Figure 4. Predicted time-averaged density on different slices at the sac volume and orifice for three injection pressures. Thermal effects are considered. The iso-surface for vapour volume fraction of 50% is included, which shows two coherent structures separated at the midplane for (b) and (c).

346

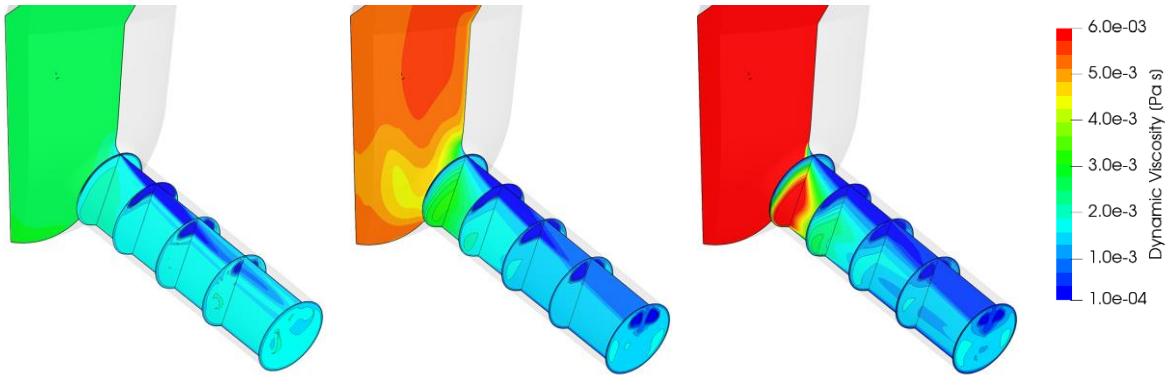

(a) 60MPa (b) 180MPa (c) 450MPa

Figure 5. Predicted time-averaged dynamic viscosity on different slices at the sac volume and orifice for three injection pressures. Thermal effects are considered.

347

348 Figure 6 shows the mass flow rate as function of the pressure drop for all cases, comparing the barotropic approach with that
349 considering thermal effects. As expected, the mass flow rate increases linearly with the square root of the difference between
350 the injection and back pressure. This shows that in neither of the two approaches the flow gets chocked with increasing
351 injection pressure. Moreover, the values for the thermal and the barotropic cases are found to be very close. Due to the
352 temperature increase, the density of the fluid drops for the thermal case, but so does the viscosity, enhancing the velocity of
353 the flow. For instance, at 180MPa the density of the thermal case is 2.9% smaller than that for the barotropic case, while the

velocities are 2.1% greater, while at 450MPa these differences are 2.1% and 1.63%, respectively. As a result, these two effects offset each other, and the predicted mass flow rate does not vary significantly between the two cases considered.

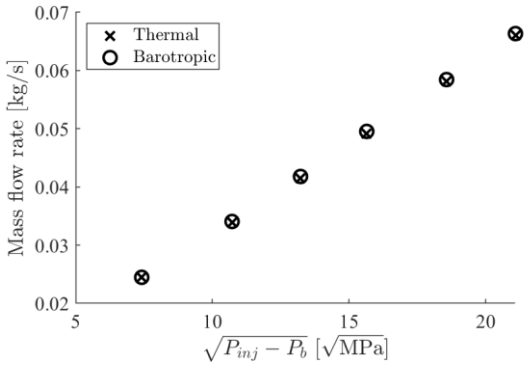

Figure 6. Mass flow rate at the orifice exit for both the barotropic and thermal cases.

3.2. Changes in temperature and vapor pressure due to thermal effects induced by wall friction and depressurisation

Figure 7 shows the relative temperature change with respect to the injection temperature, defined as:

$$\frac{T - T_{inj}}{T_{inj}} * 100 \tag{16}$$

Results are shown for the 60MPa, 180MPa and 450MPa cases, for which the injection temperature is indicated in Table 3. A solid line in the longitudinal slice shows where $T = T_{inj}$; thus, all points inside this iso-line show cooling and those outside show heating. Several observations can be made. First, as the injection pressure increases, temperature gradients increase accordingly, i.e. both lower and higher relative temperatures are found. Liquid fuel is heated up due to friction with the walls, but its temperature gradually drops towards the centre of the orifice. However, in the locations of cavitation formation inside the orifice, heating dissipation is not observed due to the vapour's significantly lower thermal conductivity and heat capacity, in addition to the significantly lower velocities observed in this region. The highest temperatures are found close to the entrance to the injection hole where the fuel fully cavitates. With respect to the injection temperature, values in this region are found to be ~5% overall higher with a local peak of 50% higher for 60MPa case; at 180MPa, the fuels heats up ~10% with a local maximum of 70%; lastly, for the 450MPa case, the highest heating of 25% is estimated, reaching a 80% local maximum. On the other hand, cooling is also enhanced with injection pressure due to liquid expansion, as seen in the core of the flow. The cooling observed is 5%, 7.5% and 10% for 60MPa, 180MPa and 450MPa, respectively.

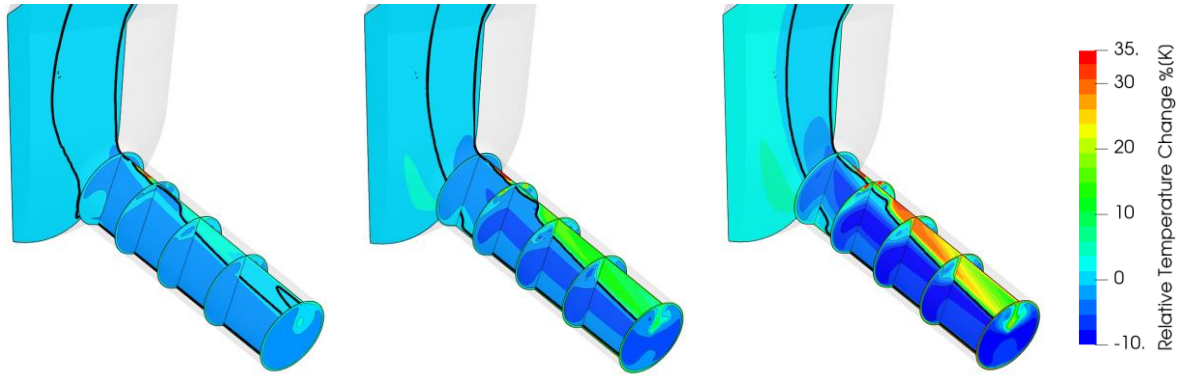

(a) 60MPa (b) 180MPa (c) 450MPa

Figure 7. Predicted time-averaged temperature change with respect to the injection temperature, defined as $(T - T_{inj})/T_{inj} * 100$, when thermal effects are considered. The injection temperature for each case is shown in Table 3. A solid thick black line is plotted in the longitudinal slice where $T = T_{inj}$, thus all points inside this iso-line show cooling and those outside show heating. Results are shown on different slices at the sac volume and orifice for three injection pressures.

375

376 Figure 8 (a) shows the temperature range for the liquid, vapour and vapour-liquid equilibrium (VLE) phases; the boiling and
377 injection temperatures are added as a reference. The range on the vapour phase is significantly higher than that for the liquid
378 phase. Maximum vapour temperatures take values of 510K, 570K and up to 640K for the 60MPa, 180MPa and 450MPa
379 pressures, respectively. For the liquid phase, heating effects are more contained: at 60MPa the liquid fuel gets heated up to
380 360K, while for 180MPa it is 410K and 504K for 450MPa; the slope of temperature increase is around 28K per 100MPa.
381 Regarding cooling, a rough correlation of a 7K of temperature decrease per 100MPa is calculated. Where the liquid and vapor
382 coexist, the temperature range is lower than for the liquid phase. The temperatures found are 325-350K for 60 MPa, 335-
383 400K for 180MPa and 355-485K for 450MPa, thus reaching a maximum temperature range of up to 130K. Figure 8 (b) shows
384 the average temperature at the orifice inlet and outlet slices. As observed, the temperature at both extremes of the orifice
385 increase with the injection pressure, due to the enhancing of the friction-induced heating. The difference in temperature
386 between these two zones also increase with the injection pressure. While the difference is of 2.3K at 60MPa, it is found to be
387 5.6K at 180MPa and 8.8K at 450MPa.

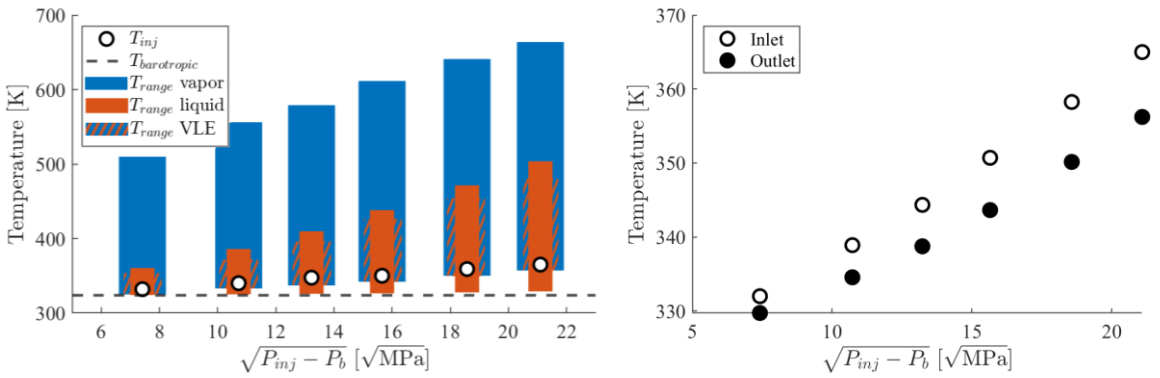

(a) (b)

Figure 8. (a) Variation in temperature for the liquid, vapor and vapor-liquid equilibrium (VLE) phases versus the square root of pressure drop. As a reference, both the injection temperature and the reference temperature used in the barotropic approach are included. (b) Average temperatures at the orifice inlet and outlet slices.

388

Figure 9 shows on the density-temperature thermodynamic diagram the distribution of predicted values in the whole computational domain; the saturation curve of the Diesel surrogate and the isentropic evolution used in the barotropic approach are also indicated. The colour of the plotted points helps identifying their location within the computational domain, i.e. in the injector inlet upstream the needle seat passage, along the needle seat passage, sac volume and inside the injector hole. For all injection pressure cases investigated, it can be clearly seen that the process is not isothermal; as shown before, the range in temperatures increases with increasing injection pressure. The flow upstream of the nozzle hole (on the right of the saturation curve) shows a smaller range in temperatures than that through the orifice, mostly following the isentropic curve with the corresponding cooling effect due to the expansion of the liquid. There are points that diverge from this isentropic curve both in the needle seat and more clearly in the sac volume, due to thermal effects. This can be clearly seen in the plot for 450MPa: the flow in the sac volume splits into two legs, one corresponding to the core of the flow cooling down due to the liquid expansion and following the isentropic curve, while the other one its heated up because of wall friction.

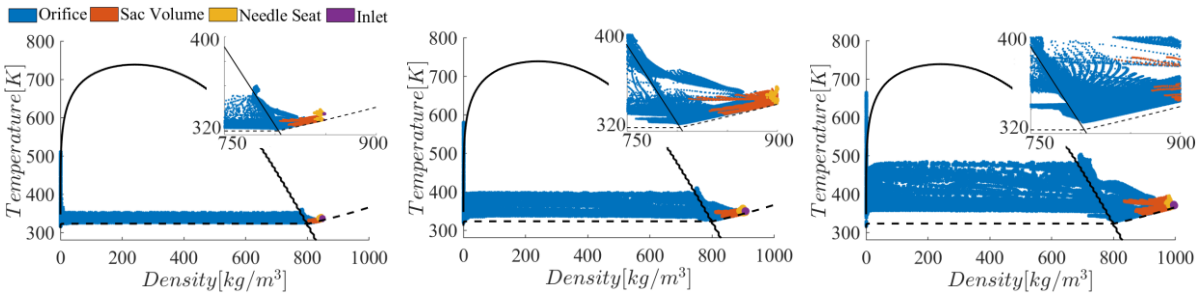

(a) 60MPa (b) 180MPa (c) 450MPa

Figure 9. Predicted time-averaged density-temperature values over the whole computational domain for three injection pressures. The saturation curve for the multicomponent Diesel surrogate (solid line) and the isentropic approach (dashed line) are indicated. The colour of the symbols distinguishes the zone in the injector they correspond to. As an inset, the distribution of point close to the saturation curve is added.

Another interesting result from the comparison between the barotropic approach and the consideration of thermal effects is shown in Figure 10. This figure shows, for a single-time instance, both the isentropic curve, and the results corresponding to thermal effects being considered. The symbols are coloured according to the value of vapor volume fraction. In all cases, the liquid phase follows the isentropic curve reasonably well at high pressures (corresponding to zones before the orifice) while diverging from it as the pressure falls during the discharge of fuel through the nozzle hole. This divergence is significantly enhanced as the injection pressure increases and therefore thermal effects become more pronounced. The distribution of points become progressively wider and shifted to higher pressures, potentially driving towards greater pressure gradients where vapour is found. As the vapour phase distribution is shifted towards greater pressures, so does the vapour pressure, shown in Figure 11 for all cases investigated; it increases with injection pressure to a substantial degree, diverging significantly from the barotropic assumption due to thermal effects. The minimum vapour pressure increases from 290Pa for 60MPa, to 523.5Pa at 180MPa and up to 1259Pa at 450MPa.

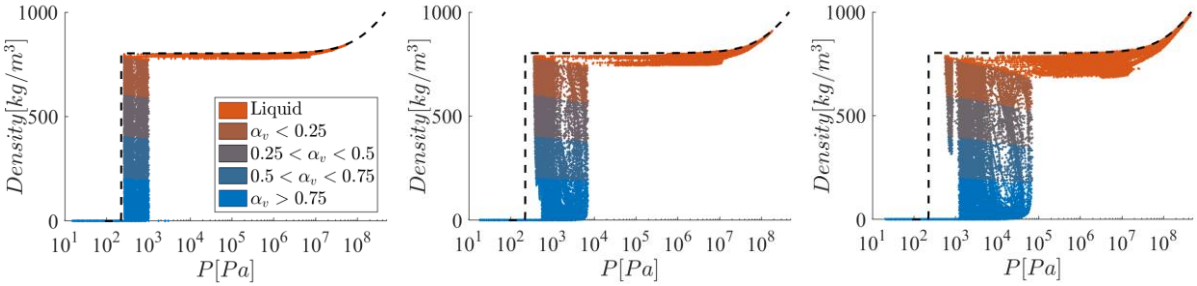

(a) 60MPa (b) 180MPa (c) 450MPa

Figure 10. Predicted single-time instance of logarithm of pressure versus density values over the whole computational domain for three injection pressures; the curve for the barotropic evolution (dashed line) is indicated. The colour of the symbols shows their value of the vapor volume fraction within different ranges.

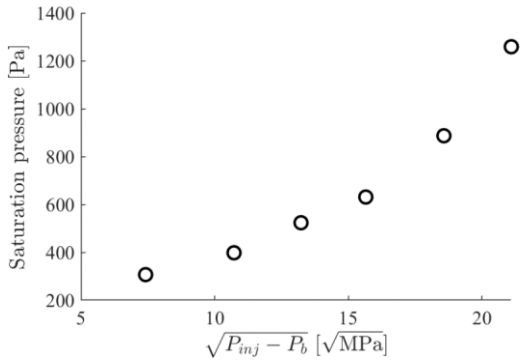

Figure 11. Predicted saturation pressure versus the square root of the pressure difference when thermal effects are considered.

3.3. Effect of injection pressure on cavitation

Figure 12 shows the time-averaged pressure distribution, in logarithmic scale, for three injection pressures on a longitudinal slice of the injector. The 50% vapour volume fraction iso-surface and the 5MPa iso-line, i.e. the back pressure value, are illustrated. As shown, the main difference between the cases is found inside the sac volume, where pressures take values of 55MPa, 162MPa and 405MPA for the 60MPa, 180MPa and 450MPa injection pressure cases, respectively. As the injection pressure increases, so does the pressure distribution inside the orifice, as indicated by the increased extent of the 5MPa iso-line within the orifice. Regarding cavitation, the iso-surface of the vaporised fuel appears to reach just slightly the orifice exit for 60MPa and vortex cavitation is produced as a detached cloud. For 180MPa and 450MPa, cavitation completely reaches the orifice exit and no vortex cavitation is observed. Moreover, the cavitation cloud for 450MPa appears to be thinner than that the 180MPa case.

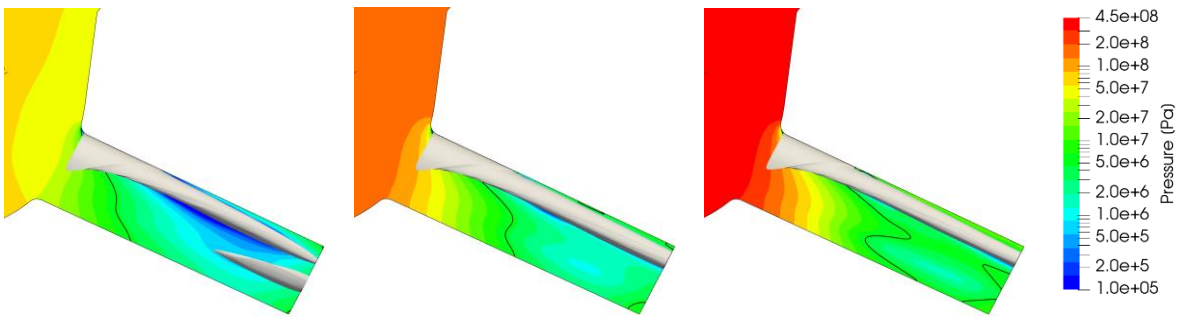

(a) 60MPa (b) 180MPa (c) 450MPa

Figure 12. Predicted time-averaged pressure on a longitudinal slice of the injector. A solid black iso-line at 5MPa, the back pressure, and the iso-surface for 50% vapour volume fraction have been included. The colour map is in logarithmic scale and thermal effects are considered.

These observations of the cavitating cloud are quantified in Figure 13(a), which shows the time-averaged vapor volume fraction inside the injector orifice versus the square root of the pressure drop. Results correspond to both the barotropic and thermal cases. As shown, the barotropic and complete formulation approaches follow similar trends. Due to the higher average temperatures and consequently higher vapour pressures found when considering thermal effects, cavitation growth is enhanced and thus found to be greater than in the barotropic approach. For both cases the volume of vapour formed inside the orifice first increases up to 120MPa and then decreases as the injection pressure increases. This is an unexpected result, as it is commonly believed that increasing the injection pressure results to higher velocities, which induce a greater boundary layer separation inside the orifice. In turn, flow separation would lead to an enhanced contraction of the flow and thus, a greater reduction in the static pressure; if this is below the local vapour pressure, more cavitation would be expected. However, the trend observed does not follow this reasoning. Figure 13(b) quantifies the % distribution of the orifice volume having pressure in three intervals: the first one for pressures above the 5MPa value of the back pressure, the second in the range [5MPa, P_v] and the last one for pressure below P_v, where cavitation is present. As seen, pressures greater than the back pressure occupy ~20% of the volume orifice at 60MPa while this percentage increases to ~55% for 450MPa. The opposite trend is observed for the other two pressure ranges; the volume with pressures below 5MPa but above the vapor pressure decreases from 65% at 60MPa down to 35% for 450MPa, while the volume occupied by pressures lower than the vapor pressure exhibits the same trend.

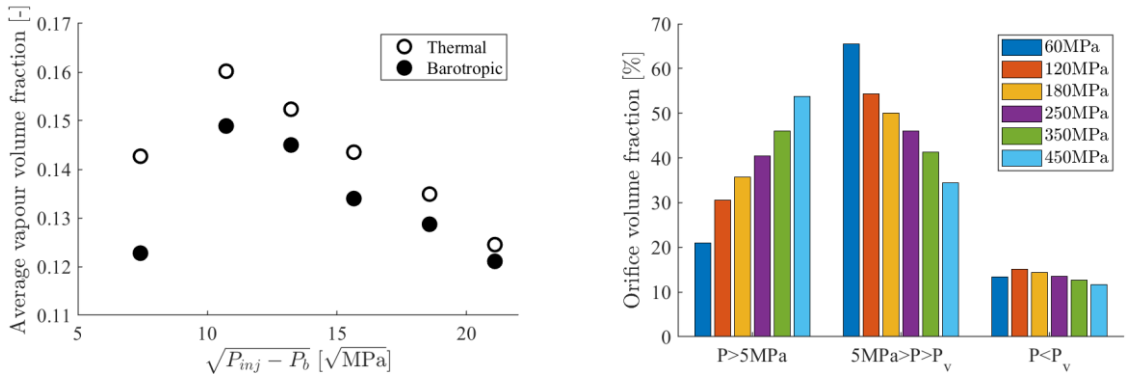

(a) (b)

Figure 13. (a) Time-averaged vapor volume fraction inside the injector orifice versus the square root of the pressure drop estimated utilising both the barotropic and thermal models. (b) Orifice volume fraction histogram for different pressure ranges inside the orifice volume when thermal effects are considered.

Various parametric studies have been performed to disprove these results as a numerical artefact; the relevant results are summarised in Figure 14 and have included injection into gas, constant fuel viscosity, non-tapering of the nozzle hole and different turbulence models such as the k-omega SST RANS model with the Reboud correction[106]. Although the absolute values of cavitation volume fraction are not the same, as cavitation is significantly dependant on the model and properties used, a similar reduction trend of cavitation volume fraction with the pressure drop is observed for all cases.

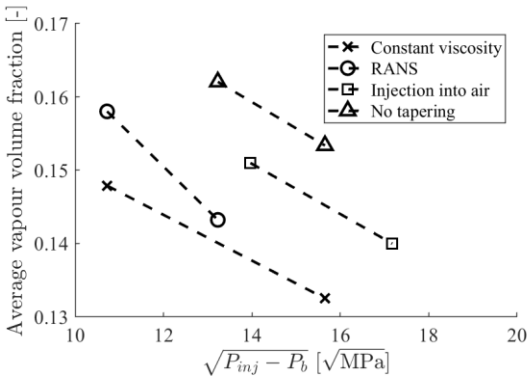

Figure 14. Effect of boundary conditions and simulation parameters on calculated vapour volume fraction as function of pressure drop.

451

452 The increased pressures found overall also affect the amount of vapour mass within the orifice, as shown in Figure 15, along
453 the orifice length for all injection pressures; results from both the barotropic and the thermal cases are indicated. Two insets
454 of the temperature distribution are added to the thermal case, corresponding to locations of high vapour mass flow rate at
455 450MPa. On the slices, an iso-line showing the location of vapour is also included. The density of the vapour fuel ρ_v is
456 calculated by the PC-SAFT EoS during the VLE calculations. As seen, as the injection pressure increases so does the flow rate
457 of vapour mass along the orifice. For instance, at 20% of the orifice length and for the thermal case, the vapour mass flow
458 rate is 0.06mg/s for 60MPa, 0.22mg/s for 180MPa and 1.02mg/s for 450MPa. However, the results for the barotropic case
459 are significantly lower. This difference can be explained because, when in vapour-liquid equilibrium, the vapour density
460 increases with temperature. For instance, at 350K the saturated vapour density is 2.5*10^{-3}kg/m^3, at 360K it increases to
461 5.03*10^{-3}kg/m^3, i.e. a 200% difference, and at 370K it doubles again to 9.9*10^{-3}kg/m^3. This can be also observed on the two
462 peaks found at approximately 40 and 75% of the orifice length, for the thermal case. In these locations, as shown by the
463 insets, a significant increase in temperature is found, which produce also an increase in the vapour density.

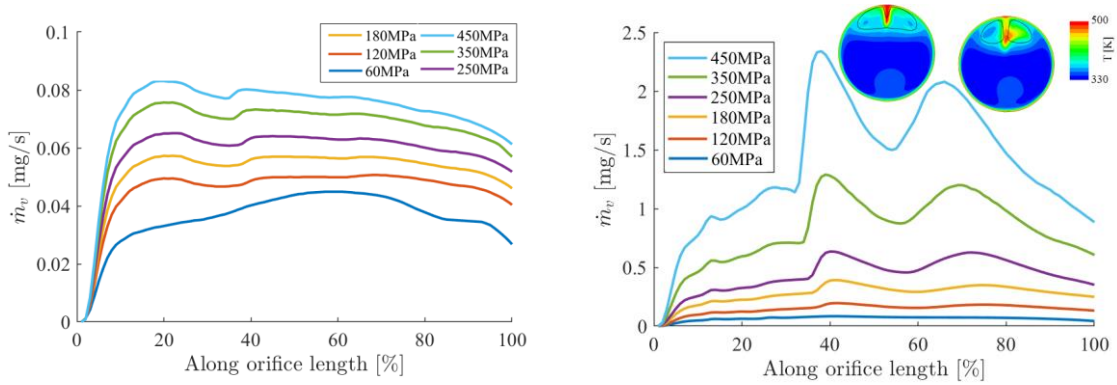

(a) Barotropic (b) Thermal

Figure 15. Time-averaged vapour mass flow rate along the orifice length for both (a) barotropic and (b) thermal cases, for all injection pressures simulated. Two insets of the temperature distribution are added to the thermal case, corresponding to locations of high vapour mass flow rate at 450MPa. On the slices, an iso-line showing the location of vapour is also depicted.

464

465 Figure 16 shows the slope of the vapour mass flow rate along the orifice length, thus presenting the locations of net
466 evaporation (positive values) and condensation (negative values) per meter of the orifice length as the fuel cavitates within
467 the nozzle hole. As already seen in Figure 15, overall values are higher in the thermal case due to the dependence of the

vapour density on temperature, particularly at 40% and 75% of the orifice length. Nevertheless, both values for evaporation and condensation are seen to increase with injection pressure for both the barotropic and the thermal cases. This is clearly shown in the thermal case by the amplitude of the observed positive and negative peaks. For instance, at the hole entrance the value for evaporation rate is 0.6g/s·m for 60MPa, 2.7g/s·m for 180MPa and 13g/s·m for 450MPa, while at ~45% of the orifice length the corresponding values for condensation are 0.07g/s·m for 60MPa, 0.62g/s·m for 180MPa and 6g/s·m for 450MPa. Moreover, while for the barotropic case most of the evaporation (values for the 450MPa case) is observed at the beginning of the orifice, with a value of 1.2g/s·m, followed by small positive values at 40% of 0.1g/s·m and of 0.01g/s·m at 60%, for the thermal case the peak in evaporation occurs at 40% of the orifice length, with a significantly higher value of 32g/s·m, followed by a smaller value of 13g/s·m at the entrance and of 7g/s·m at 60% of the orifice length.

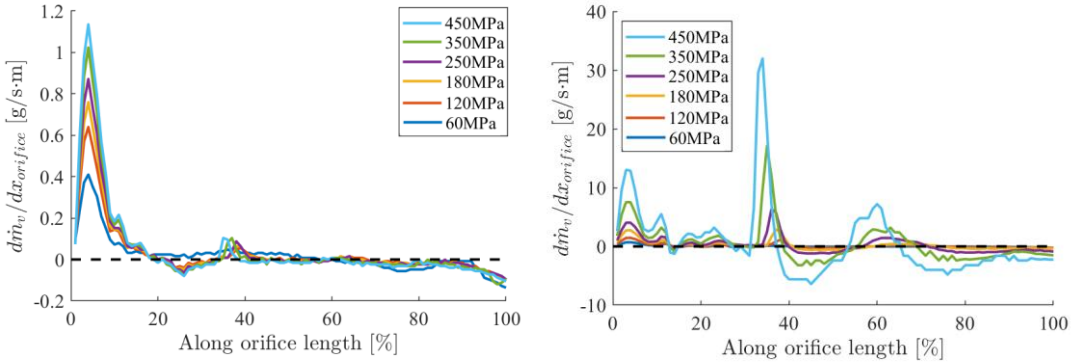

(a) Barotropic (b) Thermal

Figure 16. Slope of the vapour mass flow rate along the orifice length, showing locations of net evaporation (positive) and condensation (negative), for both the barotropic and the thermal cases. A dashed horizontal line is added at value 0, for reference.

An additional interesting finding is related to the influence of varying simultaneously the injection and back pressures on cavitation vapour volume fraction[107] but keeping the cavitation number fixed; this is defined as:

$$CN = \frac{P_{inj} - P_b}{P_b - P_{sat}} \tag{17}$$

The cavitation number chosen is 35, which corresponds to the boundary conditions of the 180MPa case. For keeping constant cavitation number, increasing the injection pressure results to increasing the back pressure and, on the other hand, decreasing the injection pressure results to decreasing back pressure. Figure 17 shows that the vapour volume fraction still decreases inside the orifice as the injection pressure increases, even by keeping constant the cavitation number. Thus, for the same injector and fluid, these results show that a constant cavitation number does not indicate a similar cavity size, but it strongly depends on the absolute value of the injection and back pressure values used.

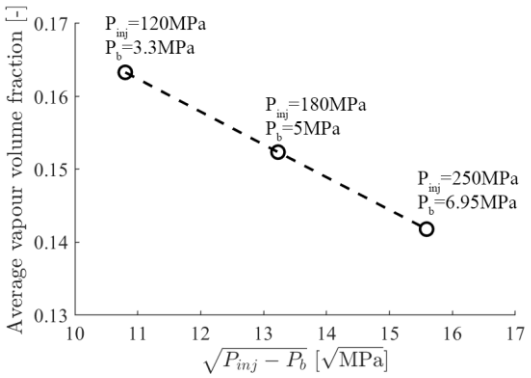

Figure 17. Time-averaged vapour volume fraction inside the injector orifice versus the square root of the pressure drop, considering thermal effects. All cases have the same cavitation number, CN=35.

3.4. Preferential cavitation

One of the benefits of using the PC-SAFT EoS coupled with a VLE algorithm is that it allows the calculation of the vaporised amount of each individual fuel component. As an example, Figure 18 shows the vapour mass fraction at 350K of the Diesel surrogate (dashed line) and of four representative components (the heaviest, lightest and two intermediates, in solid lines), as a function of the specific volume. As shown, the mixture vaporises at a variable rate as it expands, while each component vaporises as well at their distinct rhythm. The lightest component, i.e. 1,2,4-trimethylbenzene, is seen to vaporise at a higher rate than the mixture and vaporises completely considerably sooner. The heaviest one, i.e. n-octadecane, vaporises much slower than the mixture, but reaches the complete vaporisation at the same time. The intermediate components vaporise at rates in between the previous ones.

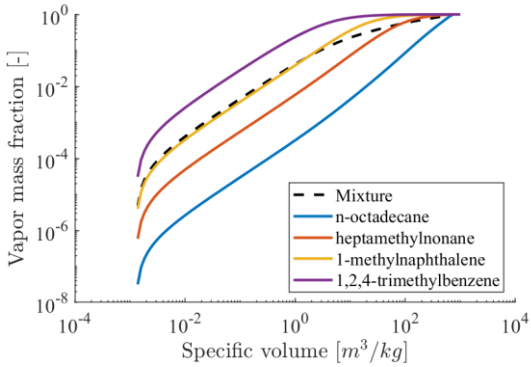

Figure 18. Vapour mass fraction of representative components of the fuel surrogate (the heaviest, lightest and two intermediate) as a function of specific volume for a 0D expansion of the fuel at 350K.

As the volume fraction per component cannot be retrieved from the equation of state, mass fractions are presented. The vaporised mass fraction of every component v_i, is calculated using the mass vapour fraction of the mixture θ, the composition of the vapour phase $\boldsymbol{x}$ and the composition of the total mixture $\boldsymbol{z}$ by:

$$v_i = \theta * x_i / z_i \tag{18}$$

Figure 19 shows iso-surfaces of the mass vapour fraction for selected components. The plotted vapour mass fraction is selected so that the iso-surface for trimethylbenzene coincides to that of the mixture 50% vapor volume fraction. As shown, trimethylbenzene is the maximum cavitating component and the heaviest one, i.e. octadecane, cavitates significantly less and mostly at the entrance of the orifice, where the flow separates, and cavitation is stronger. No significant amount of the

5 heavier components are found in the vortex cavitation cloud found at 60MPa. Moreover, as the injection pressure increases, every component is seen to cavitate further inside the cavitating cloud, observable on the iso-surface for octadecane, due to both the higher pressures and temperatures occurring in the orifice.

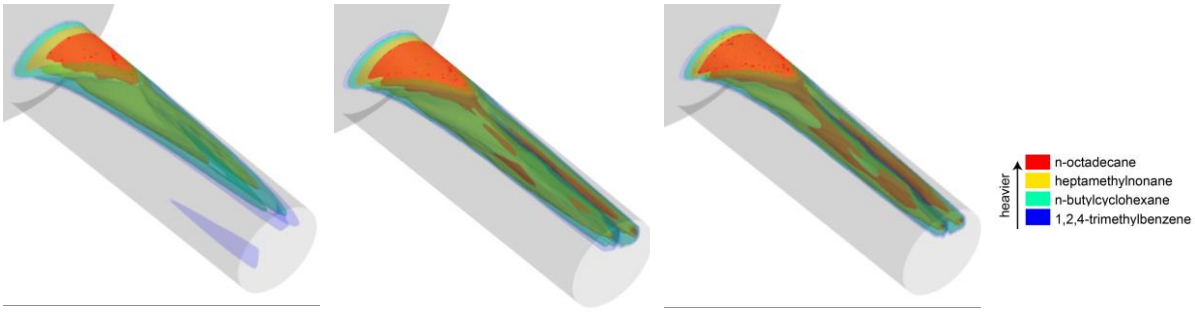

(a) 60MPa (b) 180MPa (c) 450MPa

Figure 19. Effect of the injection pressure on partial vaporisation of selected components of the Diesel surrogate simulated. Results are time-averaged and thermal effects are considered.

Figure 20 shows the mass composition of the cavitating cloud inside the orifice for all injection pressures studied while Table 5 shows the actual values. The lighter components are the ones found to be in greater amount due to their higher volatility. As seen, in all cases the 4 lightest components compose more than 75% of the vapour mass. The compound most present in the total mass of the Diesel surrogate, heptamethylnonane with 35% in mass fraction, is not the one having the highest amount of vapour phase, as it is less volatile; it's relative percentage in the vapour composition is just 3.44% at 60MPa and up to 12.5% at 450MPa. Similar observations can be drawn from octadecane, which consists 27% of the total mass of the fuel surrogate, but in the vapor cloud it is just above 1%. On the other hand, the lighter butylcyclohexane with a 11% of the total fuel mass, provides 23% and ~24% of the mass of vapor at 60MPa and 450MPa, respectively. The lightest component in the surrogate, 1,2,4-trimethylbenzene, which 5% of the initial fuel mass, when vaporises provides 23% of the total mass of vapor at 450MPa. As seen previously in Figure 16, the total mass of vapour, and as a result the mass of vapour of all components, increases with injection pressure.

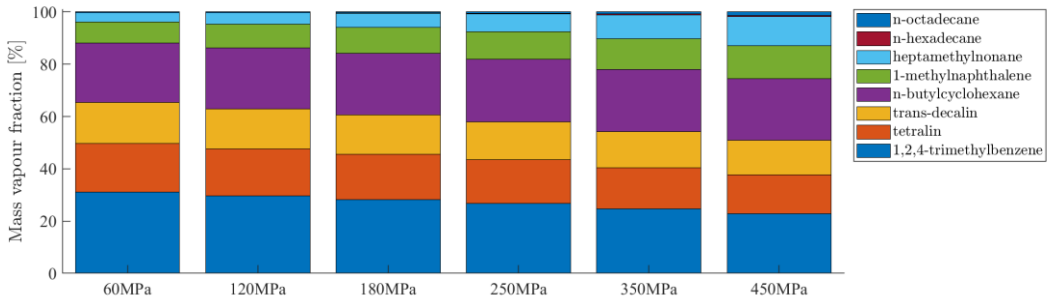

Figure 20. Time-averaged predictions for the vaporised mass composition of the vapor cloud, in a stacked fashion, for all injection pressures.

		P_{inj} [MPa]					
Component	**z [% mass]**	**60**	**120**	**180**	**250**	**350**	**450**
n-octadecane	27.308	0.2416	0.2575	0.3487	0.5068	0.8566	1.3300
n-hexadecane	3.2477	0.1050	0.1338	0.1822	0.2517	0.3784	0.5209
heptamethylnonane	35.124	3.4426	4.2924	5.3811	6.7659	8.9891	11.152
1-methylnaphthalene	10.877	8.1457	9.0432	9.8387	10.675	11.723	12.463
n-butylcyclohexane	10.815	22.619	23.278	23.589	23.805	23.807	23.550
trans-decalin	4.0392	15.721	15.431	15.051	14.601	13.894	13.232
tetralin	3.8009	18.597	18.028	17.437	16.743	15.733	14.834
1,2,4-trimethylbenzene	4.7883	31.128	29.537	28.174	26.652	24.619	22.918

Table 5. Time-averaged predictions for the vaporised mass composition of the vapor cloud, for all injection pressures. The initial surrogate mass composition is also indicated.

523

4. Summary and Conclusions

The present study is the first work reporting simulations of cavitation in a Diesel fuel injection at extreme injection pressures up to 450MPa. Additionally, it is the first work to report results using the molecular-based PC-SAFT equation of state for the modelling of the Diesel fuel properties, while has allowed for predictions of the preferential cavitation of the components in a Diesel injector to be reported for the first time. To assess the method against the common assumption of isothermal flow typically considered up to now in nozzle flow simulations, simulations considering an isentropic expansion of the fuel, and thus neglecting friction-induced thermal effects, have been also presented. Two major findings emerge from this study: (i) in-nozzle cavitation volume fraction decreases with injection pressure, although the mass of fuel cavitating increases, and (ii) each component in the surrogate cavitates at a distinct rhythm, different to that of the mixture and to that of the other components. The trend in cavitation has been explained by observing the pressure distribution within the nozzle orifice, which increase significantly with injection pressure and effectively decrease the growth of cavitation. The composition of the fuel vapour shows that the lighter components cavitate at a significantly greater amount than the heavy ones. With increasing injection pressure, all fuel components cavitate in higher mass quantities due to the higher densities of the fuel at the pressures and temperatures developing in the nozzle orifice. As a result, the mass of the total vapour fuel also increases.

Acknowledgements

This project has received funding from the European Union Horizon-2020 Research and Innovation Programme. Grant Agreement No 675528.

Nomenclature

English symbols

a	blending coefficient	$\dot{\boldsymbol{m}}$	Mass flow rate [kg/s]
C	Acoustic impedance	m	chain segment number [-]
$\boldsymbol{C_d}$	Discharge Coefficient	M	Mach number [-]
C_w	LES model constant	M_w	molar weight [g/mol]
c	Speed of sound [m/s]	P/p	Pressure [Pa]
D	diameter	R	universal gas constant [J/(kg K)]
d_{wall}	wall distance	Re	Reynolds number
E	Total energy [J/kg]	S	strain tensor
g_{ij}	abbreviation $\frac{\partial u_i}{\partial x_j}$	T	Temperature [K]
h	Enthalpy [J/kg]	t	Time [s]
k_B	Boltzmann constant	$\mathbf{u}$	Velocity [m/s]
k_{ij}	binary interaction parameter [-]	V	cell volume
k_T	Thermal conductivity [W/(m K)]	x	Vapour mass composition
κ	von Karman constant	z	Total mass composition
L	WALE LES model length scale		

Greek symbols

α_v	Volume vapour fraction	ρ	Mixture density [kg/m^3]
β	function for the hybrid flux	σ	segment diameter [Å]
λ_g	Taylor length scale	$\boldsymbol{\tau}$	Stress tensor [Pa]
μ	Dynamic viscosity [Pa.s]	θ	Mass vapour fraction [-]

Subscripts

b	Downstream conditions/boiling point	j	Coordinate direction
eff	effective, i.e. laminar plus turbulent	l	Liquid
i	component i/coordinate direction	v	Vapour
inj	At inlet conditions	t	turbulent

Superscripts

comp	compressible	L	Left side
inc	incompressible	R	Right side

Abbreviations

CN	Cavitation Number	PC-SAFT	perturbed chain statistical associating fluids theory
EoS	equation of state	*VLE*	Vapour-Liquid Equilibrium
LES	Large Eddy Simulation	WALE	Wall Adapted Large Eddy
nc	number of components		

544

545

Appendix. PC-SAFT parameters for thermodynamic and thermophysical properties

PC-SAFT parameters

	m (-)	σ (Å)	ε/k_B (K)
n-octadecane	7.438	3.948	254.90
n-hexadecane	6.669	3.944	253.59
heptamethylnonane	5.603	4.164	266.46
1-methylnaphthalene	3.422	3.901	337.14
1,2,3,4-tetrahydronaphthalene	3.088	3.996	337.46
trans-decalin	3.291	4.067	307.98
n-butylcyclohexane	3.682	4.036	282.41
1,2,4-trimethylbenzene	3.610	3.749	284.25

Table A.1. PC-SAFT parameters used in this study

Ideal gas coefficients

	A	B	C	D	ΔH_{ref} [kJ/kg]
n-octadecane	-13.474	1.71384	$-9.554*10^{-4}$	$2.03*10^{-7}$	-414.83
n-hexadecane	-11.656	1.52384	$-8.466*10^{-4}$	$1.792*10^{-7}$	-373.59
heptamethylnonane	-86.757	1.90728	$-1.3652*10^{-3}$	$3.944*10^{-7}$	-405.10
1-methylnaphthalene	-58.16	0.90672	$-6.7548*10^{-4}$	$2.014*10^{-7}$	116.94
1,2,3,4-tetrahydronaphthalene	-87.11	0.9832	$-7.1356*10^{-4}$	$2.06*10^{-7}$	27.63
trans-decalin	-127.17	1.2172	$-7.75*10^{-4}$	$1.868*10^{-7}$	-182.42
n-butylcyclohexane	-71.807	1.07592	$-6.012*10^{-4}$	$1.174*10^{-7}$	-213.32
1,2,4-trimethylbenzene	-10.6	0.66096	$-3.6292*10^{-4}$	$7.16*10^{-8}$	-13.94

Table A.2. Ideal gas parameters used during the calculation of properties

Entropy scaling parameters for viscosity

	A^{μ}	B^{μ}	C^{μ}	D^{μ}
n-octadecane	-0.94240	-4.2086	-0.92723	-0.2241
n-hexadecane	-0.89303	-3.9704	-0.84192	-0.1992
heptamethylnonane	-0.57516	-3.2643	-0.75823	-0.1992
1-methylnaphthalene	-0.59115	-2.7895	-0.58370	-0.1370
1,2,3,4-tetrahydronaphthalene	-0.50055	-2.6232	-0.44389	-0.1245
trans-decalin	-0.29640	-2.5604	-0.24863	-0.1245
n-butylcyclohexane	-0.58564	-2.8879	-0.41966	-0.1245
1,2,4-trimethylbenzene	-0.72078	-2.6213	-0.56599	-0.1121

Table A.3. Entropy Scaling parameters used for the calculation of viscosity.

Entropy scaling parameters for thermal conductivity

	A^{λ}	B^{λ}	C^{λ}	D^{λ}
n-octadecane	0	-0.40156	1.98005	0
n-hexadecane	0.36701	-0.52738	1.15300	0
heptamethylnonane	0.36701	-0.52738	1.15300	0
1-methylnaphthalene	0.51308	-0.57468	0.67839	-0.06761
1,2,3,4-tetrahydronaphthalene	0.51308	-0.57468	0.67839	-0.06761
trans-decalin	0.51308	-0.57468	0.67839	-0.06761
n-butylcyclohexane	0.51308	-0.57468	0.67839	-0.06761
1,2,4-trimethylbenzene	0	-0.45935	1.44014	0

Table A.4. Entropy Scaling parameters used for the calculation of thermal conductivity.

559 **References**
560

561 1. UNEP *The Emissions Gap Report. United Nations Environment Programme, Nairobi, page XIV and XV*; 2018.
562 2. ExxonMobil *OUTLOOK FOR ENERGY: A PERSPECTIVE TO 2040*; 2019.
563 3. Lemaire, R.; Faccinetto, A.; Therssen, E.; Ziskind, M.; Focsa, C.; Desgroux, P., Experimental comparison of soot
564 formation in turbulent flames of Diesel and surrogate Diesel fuels. *Proceedings of the Combustion Institute* **2009,** *32*, 737-
565 744.
566 4. Ribeiro, N. M.; Pinto, A. C.; Quintella, C. M.; Rocha, G. O.; Teixeira, L. S. G.; Guarieiro, L. l. L. N.; Carmo Rangel,
567 M.; Veloso, M. C. C.; Rezende, M. J. C.; Cruz, R. S.; Oliveira, A. M.; Torres, E. A.; Andrade, J. B., The Role of Additives for
568 Diesel and Diesel Blended (Ethanol or Biodiesel) Fuels: A Review. *Energy & Fuels* **2007,** *21*, 2433-2445.
569 5. Han, Z.; Uludogan, A.; Hampson, G. J.; Reitz, R. D. In *Mechanism of Soot and NOx Emission Reduction Using*
570 *Multiple-injection in a Diesel Engine*, SAE Technical Paper Series, SAE International: 1996.
571 6. Pickett, L. M.; Siebers, D. L., Soot in diesel fuel jets: effects of ambient temperature, ambient density, and injection
572 pressure. *Combustion and Flame* **2004,** *138*, 114-135.
573 7. Vera-Tudela, W.; Haefeli, R.; Barro, C.; Schneider, B.; Boulouchos, K., An experimental study of a very high-pressure
574 diesel injector (up to 5000 bar) by means of optical diagnostics. *Fuel* **2020,** *275*, 117933.
575 8. Gavaises, M., Flow in valve covered orifice nozzles with cylindrical and tapered holes and link to cavitation erosion
576 and engine exhaust emissions. *International Journal of Engine Research* **2008,** *9*, 435-447.
577 9. Payri, R.; Salvador, F. J.; Gimeno, J.; Zapata, L. D., Diesel nozzle geometry influence on spray liquid-phase fuel
578 penetration in evaporative conditions. *Fuel* **2008,** *87* (7), 1165-1176.
579 10. Schmidt, D. P.; Corradini, M. L., The internal flow of diesel fuel injector nozzles: A review. *International Journal of*
580 *Engine Research* **2001,** *2*, 1-22.
581 11. Manin, J.; Bardi, M.; Pickett, L. M.; Payri, R., Boundary condition and fuel composition effects on injection processes
582 of high-pressure sprays at the microscopic level. *International Journal of Multiphase Flow* **2016,** *83*, 267-278.
583 12. Yuan, W.; Schnerr, G. H., Numerical Simulation of Two-Phase Flow in Injection Nozzles: Interaction of Cavitation
584 and External Jet Formation. *Journal of Fluids Engineering* **2003,** *125*, 963.
585 13. Sou, A.; Hosokawa, S.; Tomiyama, A., Effects of cavitation in a nozzle on liquid jet atomization. *International Journal*
586 *of Heat and Mass Transfer* **2007,** *50*, 3575-3582.
587 14. Gavaises, M., Modeling of diesel fuel injection processes. *Ph. D. thesis, Imperial College, University of London* **1997**,
588 76-80.
589 15. Payri, R.; Molina, S.; Salvador, F. J.; Gimeno, J., A study of the relation between nozzle geometry, internal flow and
590 sprays characteristics in diesel fuel injection systems. *KSME International Journal* **2004,** *18*, 1222-1235.
591 16. Payri, R.; Salvador, F. J.; García, A.; Gil, A., Combination of visualization techniques for the analysis of evaporating
592 diesel sprays. *Energy and Fuels* **2012,** *26* (9), 5481-5490.
593 17. Reid, B.; Gavaises, M.; Mitroglou, N.; Hargrave, G.; Garner, C.; Long, E.; McDavid, R., On the formation of string
594 cavitation inside fuel injectors. *Experiments in fluids* **2014,** *55* (1), 1662.
595 18. Fitzgerald, R. P.; Vecchia, G.; Peraza, J. E.; Martin, G. C. In *Features of Internal Flow and Spray for a Multi-Hole*
596 *Transparent Diesel Fuel Injector Tip*, 29th Conference on Liquid Atomization and Spray Systems, ILASS Paris: 2019.
597 19. Yuan, W., Modeling and computation of unsteady cavitation flows in injection nozzles. *MÃcanique & Industries*
598 **2001,** *2*, 383-394.
599 20. Battistoni, M.; Som, S.; Longman, D. E., Comparison of Mixture and Multifluid Models for In-Nozzle Cavitation
600 Prediction. *Journal of Engineering for Gas Turbines and Power* **2014,** *136*, 061506.
601 21. Habchi, C.; Dumont, N.; Simonin, O., Multidimentional Simulation of Cavitating Flows in Diesel Injectors by a
602 Homogeneous Mixture Modeling Approach. *Atomization and Sprays* **2008,** *18*, 129-162.
603 22. Lindau, J. W.; Kunz, R. F.; Boger, D. A.; Stinebring, D. R.; Gibeling, H. J., High Reynolds Number, Unsteady,
604 Multiphase CFD Modeling of Cavitating Flows. *Journal of Fluids Engineering* **2002,** *124*, 607.
605 23. Singhal, A. K.; Athavale, M. M.; Li, H.; Jiang, Y., Mathematical Basis and Validation of the Full Cavitation Model.
606 *Journal of Fluids Engineering* **2002,** *124*, 617.
607 24. Karrholm, F. P.; Weller, H.; Nordin, N. In *Modelling Injector Flow Including Cavitation Effects for Diesel Applications*,
608 Volume 2: Fora, Parts A and B, ASME: 2007.
609 25. Strotos, G.; Koukouvinis, P.; Theodorakakos, A.; Gavaises, M.; Bergeles, G., Transient heating effects in high
610 pressure Diesel injector nozzles. *International Journal of Heat and Fluid Flow* **2015,** *51*, 257-267.
611 26. Theodorakakos, A.; Strotos, G.; Mitroglou, N.; Atkin, C.; Gavaises, M., Friction-induced heating in nozzle hole
612 micro-channels under extreme fuel pressurisation. *Fuel* **2014,** *123* (x), 143-150.
613 27. Cristofaro, M.; Edelbauer, W.; Koukouvinis, P.; Gavaises, M., Influence of Diesel Fuel Viscosity on Cavitating Throttle
614 Flow Simulations under Erosive Operation Conditions. *ACS omega* **2020,** *5* (13), 7182-7192.
615 28. Liu, H.; Ma, J.; Dong, F.; Yang, Y.; Liu, X.; Ma, G.; Zheng, Z.; Yao, M., Experimental investigation of the effects of
616 diesel fuel properties on combustion and emissions on a multi-cylinder heavy-duty diesel engine. *Energy Conversion and*
617 *Management* **2018,** *171*, 1787-1800.
618 29. Örley, F.; Hickel, S.; Schmidt, S. J.; Adams, N. A., Large-Eddy Simulation of turbulent, cavitating fuel flow inside a 9-
619 hole Diesel injector including needle movement. *International Journal of Engine Research* **2017,** *18* (3), 195-211.
620 30. Kolev, N., *Multiphase Flow Dynamics 3: Turbulence, Gas Absorption and Release, Diesel Fuel Properties.* Springer
621 Verlag Berlin Heidelberg: 2002.
622 31. Lemmon, E. W.; Huber, M. L.; McLinden, M. O., NIST Standard Reference Database 23: Reference Fluid
623 Thermodynamic and Transport Properties-REFPROP. 9.0. *NIST* **2010**.
624 32. Park, S. H.; Suh, H. K.; Lee, C. S., Effect of Bioethanol-Biodiesel Blending Ratio on Fuel Spray Behavior and
625 Atomization Characteristics. *Energy & Fuels* **2009,** *23*, 4092-4098.

33. Park, S. H.; Kim, S. H.; Lee, C. S., Mixing Stability and Spray Behavior Characteristics of Diesel-Ethanol-Methyl Ester Blended Fuels in a Common-Rail Diesel Injection System. *Energy & Fuels* **2009,** *23*, 5228-5235.
34. Yang, S.; Yi, P.; Habchi, C., Real-fluid injection modeling and LES simulation of the ECN Spray A injector using a fully compressible two-phase flow approach. *International Journal of Multiphase Flow* **2020,** *122*, 103145.
35. Toth, S. L., Experimental study of droplet vaporization and combustion of diesel, biodiesel and their blends in a turbulent environment at elevated pressure and temperature conditions. **2014**.
36. Zhang, L.; Kong, S. C., High-pressure vaporization modeling of multi-component petroleum-biofuel mixtures under engine conditions. *Combustion and Flame* **2011,** *158* (9), 1705-1717.
37. Strotos, G.; Gavaises, M.; Theodorakakos, A.; Bergeles, G., Numerical investigation of the evaporation of two-component droplets. *Fuel* **2011,** *90* (4), 1492-1507.
38. Abianeh, O. S.; Chen, C., A discrete multicomponent fuel evaporation model with liquid turbulence effects. *International journal of heat and mass transfer* **2012,** *55* (23-24), 6897-6907.
39. Strotos, G.; Gavaises, M.; Theodorakakos, A.; Bergeles, G., Influence of species concentration on the evaporation of suspended multicomponent droplets. *ILASS 2008* **2008**.
40. Gross, J.; Sadowski, G., Perturbed-chain SAFT: An equation of state based on a perturbation theory for chain molecules. *Industrial & engineering chemistry research* **2001,** *40*, 1244-1260.
41. Wertheim, M. S., Fluids with highly directional attractive forces. I. Statistical thermodynamics. *Journal of statistical physics* **1984,** *35*, 19-34.
42. Wertheim, M. S., Fluids with highly directional attractive forces. II. Thermodynamic perturbation theory and integral equations. *Journal of statistical physics* **1984,** *35*, 35-47.
43. Wertheim, M. S., Fluids with highly directional attractive forces. III. Multiple attraction sites. *Journal of statistical physics* **1986,** *42*, 459-476.
44. Wertheim, M. S., Fluids with highly directional attractive forces. IV. Equilibrium polymerization. *Journal of statistical physics* **1986,** *42*, 477-492.
45. De Villiers, A.; Schwarz, C.; Burger, A.; Kontogeorgis, G., Evaluation of the PC-SAFT, SAFT and CPA equations of state in predicting derivative properties of selected non-polar and hydrogen-bonding compounds. *Fluid Phase Equilibria* **2013,** *338*, 1–15.
46. Leekumjorn, S.; Krejbjerg, K., Phase behavior of reservoir fluids: Comparisons of PC-SAFT and cubic EOS simulations. *Fluid Phase Equilibria* **2013,** *359*, 17–23.
47. Peng, D.-Y.; Robinson, D. B., A new two-constant equation of state. *Industrial & Engineering Chemistry Fundamentals* **1976,** *15*, 59-64.
48. Soave, G., Equilibrium constants from a modified Redlich-Kwong equation of state. *Chemical Engineering Science* **1972,** *27*, 1197-1203.
49. Yan, W.; Varzandeh, F.; Stenby, E. H., PVT modeling of reservoir fluids using PC-SAFT EoS and Soave-BWR EoS. *Fluid Phase Equilibria* **2015,** *386*, 96-124.
50. Burgess, W. A.; Tapriyal, D.; Morreale, B. D.; Soong, Y.; Baled, H. O.; Enick, R. M.; Wu, Y.; Bamgbade, B. A.; McHugh, M. A., Volume-translated cubic EoS and PC-SAFT density models and a free volume-based viscosity model for hydrocarbons at extreme temperature and pressure conditions. *Fluid Phase Equilibria* **2013,** *359*, 38–44.
51. Schou Pedersen, K.; Hasdbjerg, C. In *PC-SAFT equation of state applied to petroleum reservoir fluids*, SPE Annual Technical Conference and Exhibition, 2007.
52. Gord, M. F.; Roozbahani, M.; Rahbari, H. R.; Hosseini, S. J. H., Modeling thermodynamic properties of natural gas mixtures using perturbed-chain statistical associating fluid theory. *Russian Journal of Applied Chemistry* **2013,** *86*, 867–878.
53. Mueller, C. J.; Cannella, W. J.; Bays, J. T.; Bruno, T. J.; DeFabio, K.; Dettman, H. D.; Gieleciak, R. M.; Huber, M. L.; Kweon, C.-B.; McConnell, S. S.; Pitz, W. J.; Ratcliff, M. A., Diesel Surrogate Fuels for Engine Testing and Chemical-Kinetic Modeling: Compositions and Properties. *Energy & Fuels* **2016,** *30*, 1445-1461.
54. Vidal, A.; Rodriguez, C.; Koukouvinis, P.; Gavaises, M.; McHugh, M. A., Modelling of Diesel fuel properties through its surrogates using Perturbed-Chain, Statistical Associating Fluid Theory. *International Journal of Engine Research* **2019**.
55. *OpenFOAM*, v2.4.
56. Payri, R.; Tormos, B.; Gimeno, J.; Bracho, G., The potential of Large Eddy Simulation (LES) code for the modeling of flow in diesel injectors. *Mathematical and Computer Modelling* **2010,** *52* (7-8), 1151-1160.
57. Koukouvinis, P.; Naseri, H.; Gavaises, M., Performance of turbulence and cavitation models in prediction of incipient and developed cavitation. *International Journal of Engine Research* **2017,** *18* (4), 333-350.
58. Nicoud, F.; Ducros, F., Subgrid-scale stress modelling based on the square of the velocity gradient tensor. *Flow, turbulence and Combustion* **1999,** *62* (3), 183-200.
59. Koukouvinis, P.; Gavaises, M.; Li, J.; Wang, L., Large Eddy Simulation of Diesel injector including cavitation effects and correlation to erosion damage. *Fuel* **2016,** *175*, 26-39.
60. Liu, F. *A Thorough Description Of How Wall Functions Are Implemented In OpenFOAM*; 2016; pp 1-30.
61. Gross, J.; Sadowski, G., Perturbed-Chain SAFT: An Equation of State Based on a Perturbation Theory for Chain Molecules. *Industrial & Engineering Chemistry Research* **2001,** *40* (4), 1244-1260.
62. Vidal, A.; Koukouvinis, P.; Gavaises, M., Vapor-liquid equilibrium calculations at specified composition, density and temperature with the perturbed chain statistical associating fluid theory (PC-SAFT) equation of state. *Fluid Phase Equilibria* **2020**, 112661.
63. Saurel, R.; Petitpas, F.; Abgrall, R., Modelling phase transition in metastable liquids: application to cavitating and flashing flows. *Journal of Fluid Mechanics* **2008,** *607*, 313-350.
64. Lötgering-Lin, O.; Gross, J., Group Contribution Method for Viscosities Based on Entropy Scaling Using the Perturbed-Chain Polar Statistical Associating Fluid Theory. *Industrial and Engineering Chemistry Research* **2015,** *54* (32), 7942-7952.

65. Beattie, D.; Whalley, P., A simple two-phase frictional pressure drop calculation method. *International Journal of Multiphase Flow* **1982,** *8* (1), 83-87.
66. Hopp, M.; Gross, J., Thermal Conductivity of Real Substances from Excess Entropy Scaling Using PCP-SAFT. *Industrial and Engineering Chemistry Research* **2017,** *56* (15), 4527-4538.
67. Koukouvinis, P.; Gavaises, M. In *Simulation of throttle flow with two phase and single phase homogenous equilibrium model*, Journal of Physics: Conference Series, IOP Publishing: 2015; p 012086.
68. Karathanassis, I.; Trickett, K.; Koukouvinis, P.; Wang, J.; Barbour, R.; Gavaises, M., Illustrating the effect of viscoelastic additives on cavitation and turbulence with X-ray imaging. *Scientific reports* **2018,** *8* (1), 1-15.
69. Karathanassis, I. K.; Koukouvinis, P.; Kontolatis, E.; Lee, Z.; Wang, J.; Mitroglou, N.; Gavaises, M., High-speed visualization of vortical cavitation using synchrotron radiation. *Journal of Fluid Mechanics* **2018,** *838*, 148-164.
70. Papoutsakis, A.; Theodorakakos, A.; Giannadakis, E.; Papoulias, D.; Gavaises, M. *LES predictions of the vortical flow structures in diesel injector nozzles*; 0148-7191; SAE Technical Paper: 2009.
71. Reid, B. A.; Hargrave, G. K.; Garner, C. P.; Wigley, G., An investigation of string cavitation in a true-scale fuel injector flow geometry at high pressure. *Physics of Fluids* **2010,** *22* (3), 031703.
72. Brunhart, M.; Soteriou, C.; Daveau, C.; Gavaises, M.; Koukouvinis, P.; Winterbourn, M., Cavitation erosion risk indicators for a thin gap within a diesel fuel pump. *Wear* **2020,** *442*, 203024.
73. Theodorakakos, A.; Mitroglou, N.; Gavaises, M., Simulation of heating effects caused by fuel pressurisation at 3000bar in Diesel fuel injectors. *11th Engine Combustion Processes, Germany* **2013**.
74. Theodorakakos, A.; Strotos, G.; Gavaises, M.; Koukouvinis, P., Quantification of Friction-induced Heating in tapered Diesel orifices. *SIA International Conference on Diesel Powertrains, France* **2014**.
75. Strotos, G.; Theodorakakos, A.; Gavaises, M.; Koukouvinis, P.; Wang, L.; Li, J.; McDavid, R. M., Fuel heating in high pressure diesel nozzles. *Conference on Thermo- and Fluid-Dynamic Processes in Diesel Engines, Spain* **2014**.
76. Salemi, R.; Koukouvinis, P.; Strotos, G.; McDavid, R.; Wang, L.; Li, J.; Marengo, M.; Gavaises, M. In *Evaluation of friction heating in cavitating high pressure Diesel injector nozzles*, Journal of Physics: Conference Series, IOP Publishing: 2015; p 012083.
77. Salemi, R.; McDavid, R.; Koukouvinis, P.; Gavaises, M.; Marengo, M. In *Steady State and Transient, Non-isothermal Modeling of Cavitation in Diesel Fuel Injectors*, Proceedings of ILASS Americas 27th Annual Conference on Liquid Atomization and Spray Systems, Raleigh, NC, May, 2015.
78. Vidal, A.; Rodriguez, C.; Koukouvinis, P.; Gavaises, M.; McHugh, M. A., Modelling of Diesel fuel properties through its surrogates using Perturbed-Chain, Statistical Associating Fluid Theory. *International Journal of Engine Research* **2018**, 146808741880171.
79. Rowane, A. J.; Mahesh Babu, V.; Rokni, H. B.; Moore, J. D.; Gavaises, M.; Wensing, M.; Gupta, A.; McHugh, M. A., Effect of Composition, Temperature, and Pressure on the Viscosities and Densities of Three Diesel Fuels. *Journal of Chemical & Engineering Data* **2019,** *64* (12), 5529-5547.
80. Rokni, H. B.; Moore, J. D.; Gupta, A.; McHugh, M. A.; Mallepally, R. R.; Gavaises, M., General method for prediction of thermal conductivity for well-characterized hydrocarbon mixtures and fuels up to extreme conditions using entropy scaling. *Fuel* **2019,** *245*, 594-604.
81. Rokni, H. B.; Gupta, A.; Moore, J. D.; McHugh, M. A.; Bamgbade, B. A.; Gavaises, M., Purely predictive method for density, compressibility, and expansivity for hydrocarbon mixtures and diesel and jet fuels up to high temperatures and pressures. *Fuel* **2019,** *236*, 1377-1390.
82. Cristofaro, M.; Edelbauer, W.; Koukouvinis, P.; Gavaises, M., A numerical study on the effect of cavitation erosion in a diesel injector. *Applied Mathematical Modelling* **2020,** *78*, 200-216.
83. Cristofaro, M.; Edelbauer, W.; Gavaises, M.; Koukouvinis, P. In *Numerical simulation of compressible cavitating two-phase flows with a pressure-based solver*, 28TH CONFERENCE ON LIQUID ATOMIZATION AND SPRAY SYSTEMS, ILASS-EUROPE 2017, 2017.
84. Caupin, F.; Stroock, A. D., The stability limit and other open questions on water at negative pressure. *Liquid Polymorphism: Advances in Chemical Physics* **2013,** *152*, 51-80.
85. Trevena, D., Cavitation and the generation of tension in liquids. *Journal of Physics D: Applied Physics* **1984,** *17* (11), 2139.
86. Schnerr, G. H.; Sauer, J., Physical and Numerical Modeling of Unsteady Cavitation Dynamics. *Fourth International Conference on Multiphase Flow* **2001,** (May 2001), 1-12.
87. Singhal, A. K.; Athavale, M. M.; Li, H.; Jiang, Y., Mathematical Basis and Validation of the Full Cavitation Model. *Journal of Fluids Engineering* **2002,** *124* (3), 617-617.
88. Zwart, P. J.; Gerber, A. G.; Belamri, T. In *A two-phase flow model for predicting cavitation dynamics*, Fifth international conference on multiphase flow, Yokohama, Japan, 2004.
89. Naseri, H.; Trickett, K.; Mitroglou, N.; Karathanassis, I.; Koukouvinis, P.; Gavaises, M.; Barbour, R.; Diamond, D.; Rogers, S. E.; Santini, M., Turbulence and Cavitation Suppression by Quaternary Ammonium Salt Additives. *Scientific reports* **2018,** *8* (1), 1-15.
90. Dumond, J.; Magagnato, F.; Class, A., Stochastic-field cavitation model. *Physics of Fluids* **2013,** *25* (7), 073302.
91. Giannadakis, E.; Gavaises, M.; Arcoumanis, C., Modelling of cavitation in diesel injector nozzles. *Journal of Fluid Mechanics* **2008,** *616*, 153-193.
92. Arabnejad, M. H.; Amini, A.; Farhat, M.; Bensow, R. E., Numerical and experimental investigation of shedding mechanisms from leading-edge cavitation. *International Journal of Multiphase Flow* **2019,** *119*, 123-143.
93. Ghahramani, E.; Arabnejad, M. H.; Bensow, R. E., A comparative study between numerical methods in simulation of cavitating bubbles. *International Journal of Multiphase Flow* **2019,** *111*, 339-359.

94. Giannadakis, E.; Papoulias, D.; Theodorakakos, A.; Gavaises, M., Simulation of cavitation in outward-opening piezo-type pintle injector nozzles. *Proceedings of the Institution of Mechanical Engineers, Part D: Journal of Automobile Engineering* **2008,** *222* (10), 1895-1910.
95. Kedrinskiy, V. K., *Hydrodynamics of Explosion: experiments and models*. Springer Science & Business Media: 2006.
96. Wang, C.; Moro, A.; Xue, F.; Wu, X.; Luo, F., The influence of eccentric needle movement on internal flow and injection characteristics of a multi-hole diesel nozzle. *International Journal of Heat and Mass Transfer* **2018,** *117*, 818-834.
97. Nurick, W. H., Orifice Cavitation and Its Effect on Spray Mixing. *Journal of Fluids Engineering* **1976,** *98*, 681.
98. Gavaises, M.; Andriotis, A.; Papoulias, D.; Mitroglou, N.; Theodorakakos, A., Characterization of string cavitation in large-scale Diesel nozzles with tapered holes. *Physics of Fluids* **2009,** *21*, 052107.
99. Mitroglou, N.; McLorn, M.; Gavaises, M.; Soteriou, C.; Winterbourne, M., Instantaneous and ensemble average cavitation structures in Diesel micro-channel flow orifices. *Fuel* **2014,** *116*, 736-742.
100. Mitroglou, N.; Gavaises, M., Mapping of cavitating flow regimes in injectors for medium-/heavy-duty diesel engines. *International Journal of Engine Research* **2013,** *14* (6), 590-605.
101. Mitroglou, N.; Gavaises, M., Cavitation inside Real-Size Fully Transparent Fuel Injector Nozzles and Its Effect on Near-Nozzle Spray Formation. *Proc. ofWorkshop on Droplet Impact Phenomena and Spray Investigations (DIPSI), University of Bergamo, Italy* **2011**.
102. Santos, E. G.; Shi, J.; Gavaises, M.; Soteriou, C.; Winterbourn, M.; Bauer, W., Investigation of cavitation and air entrainment during pilot injection in real-size multi-hole diesel nozzles. *Fuel* **2020,** *263*, 116746.
103. Gold, M.; Pearson, R.; Turner, J.; Sykes, D.; Stetsyuk, V.; De Sercey, G.; Crua, C.; Koukouvinis, F.; Gavaises, M., Simulation and Measurement of Transient Fluid Phenomena within Diesel Injection. *SAE Technical Papers* **2019,** *2019*, 0066.
104. Zhang, L.; He, Z.; Guan, W.; Wang, Q.; Som, S., Simulations on the cavitating flow and corresponding risk of erosion in diesel injector nozzles with double array holes. *International Journal of Heat and Mass Transfer* **2018,** *124*, 900-911.
105. Mueller, C. J.; Cannella, W. J.; Bays, J. T.; Bruno, T. J.; Defabio, K.; Dettman, H. D.; Gieleciak, R. M.; Huber, M. L.; Kweon, C.-B. B.; McConnell, S. S.; Pitz, W. J.; Ratcliff, M. A., Diesel Surrogate Fuels for Engine Testing and Chemical-Kinetic Modeling: Compositions and Properties. *Energy and Fuels* **2016,** *30* (2), 1445-1461.
106. Fortes Patella, R.; Choffat, T.; Reboud, J. L.; Archer, A., Mass loss simulation in cavitation erosion: Fatigue criterion approach. *Wear* **2013,** *300* (1-2), 205-215.
107. Brennen, C. E., *Cavitation and bubble dynamics*. 2013; p 1-249.